Study of Nanoparticles of SnO_2 on Au and Nanoparticles of TiO_2 on Ag for Plasmonic Applications

Nader Seirafianpour

A Thesis

in

The Department

of

Electrical and Computer Engineering

Presented in Partial Fulfillment of the Requirements

for the Degree of Master of Applied Science (Electrical and Computer Engineering) at

Concordia University

Montreal, Quebec, Canada

August, 2007

Your file Votre référence
ISBN: 978-0-494-34776-8
Our file Notre référence
ISBN: 978-0-494-34776-8

Abstract

Study of Nanoparticles of SnO_2 on Au and Nanoparticles of TiO_2 on Ag for Plasmonic Applications

Nader Seirafianpour

Nanolayered systems composed of a gold film coated by a granular tin dioxide layer, and a silver film coated by a granular layer of titanium dioxide are fabricated by combined sputtering/sol-gel methods. The conditions of the sol-gel synthesis and the substrate materials were adjusted with a particular attention to the aggregation effects, especially in the case of the gold/tin dioxide system. The dielectric particles are uniformly distributed on the metal surfaces and the films are smooth (mean roughness less than 6 nm). The components of the nanolayered systems prepared in this work are found to be crystalline and the sputtered metal is preferentially oriented on the substrate. Because of the low-temperature sol-gel method used for the synthesis, especially small (4-5 nm) crystallites of titanium dioxide (anatase allotropic phase) have been found with a narrow size distribution. Size and intensity enhancement effects have been evidenced in both systems and studied by micro-Raman spectroscopy.

A particular attention is paid in this work to the optical properties of the nanolayered composites with an emphasis on the surface plasmon resonance. The near-normal reflection spectra are measured and the effect of the dielectric coating on both the surface plasmon band of the noble metal and the band gap absorption of the dielectric are investigated. The effective-medium theory is used

to calculate the reflection curves. The simulated curves show a qualitative agreement with the experimental spectra. The possibility to use these systems in sensing applications is discussed.

Acknowledgements

I would like to thank all people who supported me to complete this thesis and who cannot all be named here.

First, I would like to thank my thesis supervisor, Professor Vo-Van Truong, who has suggested the topic of this thesis and whose knowledge and guidance have helped me to shape my research skills. I thank him for his patience and encouragement that carried me on through difficult times.

I owe my deep regards to Dr. Simona Badilescu, who has provided me with much information and support in all different parts of this research. She taught me how to apply my skills in a new way, and led me to the world of nanoscience materials.

I am grateful to my first supervisor, Prof. Victor Rossokhaty, who unfortunately has passed away. He introduced me to my previous thesis topic that had to change in the circumstances. His visionary thoughts and energetic working style have influenced me greatly.

I also thank Prof. Mojtaba Kahrizi, who advised, taught, and helped me in various aspects of my research and master program. He is the one that I can always count on to discuss the tiniest details of a problem.

I would like to make a special mention of Dr. Laszlo Kalman from the Physics Department for giving me access to his equipment and for his kindness.

Many thanks to Dr. Y. Djaoued from the Universite' de Moncton and to Dr. R. Bruning from Mount Allison University for their help.

Finally, without the support of my lovely wife, daughter, and parents, I would never have succeeded. I hope they will enjoy the effort being completed.

Table of Contents

List of Figures

List of Tables

List of Publications and Conference Contributions

1. N. Seirafianpour, S. Badilescu, Y. Djaoued, R. Brüning, S. Balaji, M. Kahrizi and V.-V Truong, "Optical Properties of Low Temperature Prepared Granular Titanium Dioxide on Smooth Silver Substrates," Thin Solid Films, submitted.
2. N. Seirafianpour, S. Badilescu, R. Bruning, Y. D. Djaoued, S. Balaji, M. Kahrizi, and V.-V. Truong, "Optical Properties of Tin Dioxide-Coated Nanocrystalline Gold Films," Thirteenth Canadian Semiconductor Technology Conference, Montreal, Canada (2007).
3 S. Badilescu, N. Seirafianpour, A.-R. Hajiaboli, Y. D. Djaoued, M. Kahrizi, P. V. Ashrit, and V.-V. Truong, "Fabrication of Ordered Films of Polystyrene-Gold Composites by a New Flow-Controlled Method," J. Mater. Sci. Mater. Electron. **18**, 383 (2007).
4 S. Badilescu, A.-R. Hajiaboli, N. Seirafianpour, R. Sadeghian , M. Kahrizi, and V.-V. Truong, "Study of the Structural Evolution within Polystyrene and Polystyrene-Gold Composite Colloidal Crystals by AFM and SEM," Appl. Phys. Lett. **90**, 23113 (2007).
5 Y. D. Djaoued, S. Badilescu, N. Seirafianpour, A.-R. Hajiaboli, R. B. Sadeghian, K. Bradley, R. Bruning, M. Kahrizi, and V.-V. Truong, " A Micro-Raman Spectroscopy Study of Colloidal Crystal Films of Polystyrene-Gold Composites," Appl. Spectrosc. accepted for publication.

Chapter 1: Introduction

In recent years, there has been a growing interest in the development of new nanomaterials with tailored optical characteristics to provide the basis for the emerging new technologies. Enhanced and /or novel optical properties can be achieved in a diverse range of composite materials [1]. Advanced thin film deposition techniques allow today the fabrication of high-quality nanocomposites having a wide range of compositions and phases. They range from multilayered materials composed of layers of different phases, generally known as heterostructures to nanofilamentary and nanowire composites and nanoparticulate composites. This last category defines a very important class of materials composed of nanoscale metal particles, generally Au or Ag, embedded in a ceramic or semiconductor matrix. In the early 70s, it has been shown that the electrical and optical properties of this particular kind of nanosystem strongly depend on the composition [2]. For example, in the case of Ag-SiO_2 and Au-SiO_2 films with less than 50% SiO_2, the structure consists of amorphous dielectric inclusions in a continuous metal matrix while for more than 50% SiO_2, separate metallic particles are dispersed in an amorphous SiO_2 continuum. The properties of the two materials forming a metal-dielectric interface determine its reflectivity and its ability to support SPP (surface plasmon polariton) waves associated with the collective oscillation of the conduction electrons.

Silver and gold films have attracted a wide interest due to unique optical properties and their potential applications in optical devices, chemical and biological sensors, and surface-enhanced Raman spectroscopy (SERS) [3]. Surface plasmon resonance (SPR) excitation can dramatically enhance the local

EM field, which plays a key role in surface-enhanced Raman spectroscopy (SERS). Why is it desirable to be able to control the SPR frequency? One of the motivations comes from SERS, in which the excitation and emission frequencies must overlap the SPR frequency of the substrate. In the visible region, silver and gold-coated substrates have the right SPR frequency and have been widely used. Today, however, SERS is commonly practiced with a wider range of excitation wavelength from UV to near-IR and therefore, it is important to be able to tune and extend the metal SPR frequency. The ability to control the optical properties, especially the tunability in SPR, offers numerous opportunities in optical signal processing and diverse sensing applications. Indeed, the high sensitivity of SPR to the local dielectric environment, has attracted a great deal of interest for diverse sensing applications. For example, SPR spectroscopy based on thin gold films on glass, is fast becoming the most important (and commercially most successful) method for affinity biosensing.

In this work, we have investigated the SPR in a nanosystem composed of a transparent granular dielectric film deposited on a smooth metallic surface. Vo-Van Truong et al. [4], [5], [6] have demonstrated that in such a system, the excitation of surface plasma waves is possible via mirror image effects between the particles and the metallic substrate. This coupling mechanism provides a new tool for study of surface plasmons and has been used here in order to investigate two particularly important nanosystems: gold-tin dioxide (Au/SnO_2) and silver-titanium dioxide (Ag/TiO_2). The choice of the materials is dictated by the great scientific and technological interest of tin dioxide in fields such as optoelectronics, photothermal conversion of energy and gas sensing; noble metal

nanocomposites of TiO_2 have recently emerged as one of the most important candidates for photoelectrochemical applications. For the fabrication of these nanosystems, combined sputtering/sol-gel methods have been developed. The sol-gel methods used here present many advantages compared to sputtering methods used earlier, such as excellent homogeneity, thickness control and the possibility to coat large and complex surfaces at a rather low cost. In addition, as far as the structure and morphology are concerned, the material composition and phase are precisely controlled.

The interrelation between the nanosystem's properties and the preparation and heat-treatment conditions was investigated in detail, with particular attention to the aggregation processes, especially for the Au/SnO_2 system. To this regard, special emphasis was given to the morphology and the resulting optical properties as probed by the characterization techniques such as atomic force microscopy (AFM), X-ray diffraction, micro-Raman spectroscopy and UV-visible spectroscopy.

The theoretical reflection curves have been calculated for both systems using an effective medium approach and compared to the experimental optical properties. By combining chemical fabrication methods (sol-gel dip-coating) with computational effective medium modeling, a variety of metallo-dielectric nanoparticle-based systems that support SPR at specifically wavelengths can be designed.

Thesis Layout

Chapter 1: Introduction

The nanocomposite materials are briefly described with an emphasis on nanosystems containing gold and silver in conjunction with a dielectric material. Surface plasmon resonance (SPR) in these systems and its importance in various fields are stressed. The nanosystems investigated in this work and the techniques used for their fabrication are described.

Chapter 2: Theoretical Considerations

The theoretical background of the phenomenon of SPR and the most important methods to excite them in noble metals and their composites are described. In particular, an effective medium theory used for the simulation of the optical properties is discussed.

Chapter 3: Characterization Methods and Measurements

The instruments and the methods used for the structural (XRD), compositional (micro-Raman- and FTIR spectroscopy), morphological (AFM) and optical (UV-visible spectroscopy) characterization of the nanosystems are described.

Chapter 4: Sample Preparation

The fabrication of the materials is described in some detail. The sputtering method and the parameters used for the deposition of Au and Ag are given. The sol-gel approach and the chemistry involved in it are given and the dip-coating method and apparatus are described.

Chapter 5: Results and Discussion

The results related to the morphological and optical properties of the

nanosystems are shown and discussed in detail. The AFM size distributions are presented and discussed for each of the nanosystems. The effect of the thermal annealing of the Au/SnO_2 on the morphology and the optical properties are studied and discussed in detail. The simulated reflectivity curves are presented and compared to the experimental curves.

Chapter 6: Conclusions and Future Directions

This chapter contains a summary of the work. The most important results obtained in this work are emphasized and some directions for future work are suggested.

Chapter 2: Theoretical Considerations

2.1 Surface Plasmons

Surface plasmon polaritons are the electromagnetic waves that propagate along the surface between a metal and a dielectric. These waves are confined at the surface because of their interaction with the free electrons of the metallic medium that resonate collectively with the light waves. The metals that exhibit this phenomenon comprise noble metals such as silver (Ag) and gold (Au), alkali metals like manganese (Mg) and Aluminum (Al), or other metals such as copper (Cu), titanium (Ti), and chromium (Cr) [7].

These surface plasmon waves can be excited by light under specific conditions. Depending on the metallic surface structures, there are two groups of surface plasmon resonance:

1. Surface plasmon resonance (SPR) for planar surfaces.
2. Localized surface plasmon resonance (LSPR) for nanoscale metallic structures.

Since an impinging light on the surface of some metals like silver and gold has less than 50 nm penetration, the electrons in this surface play a most significant role. In order to define the excitation and resonance of the surface plasmons for a metal film, the Drude-Lorentz model can be considered. In this model, the metal film is viewed as a plasma with the metal nuclei as positive ions at fixed positions surrounded by a cloud of free electrons [8].

2.2 Excitation of Surface Plasma Waves

When light is incident onto a media composed of a dielectric incident medium and a metal substrate with refractive indices n_1, n_2 and dielectric

functions ε_1, ε_2 respectively, the light wave is split into a reflected wave and a transmitted wave characterized by the following [9].

$$K_i = K_r = \frac{\omega}{c}\sqrt{\varepsilon_1} = \frac{\omega}{c}n_1 \tag{2.1}$$

$$K_t = \frac{\omega}{c}\sqrt{\varepsilon_2} = \frac{\omega}{c}n_2 \tag{2.2}$$

where c = speed of light in vacuum

K_i = modulus of wave vector of incident light

K_r= modulus of wave vector of reflected light

K_t = modulus of wave vector of transmitted light

The frequency dependence of ε_2 can be taken into account and equation (2.2) can be rewritten as:

$$K_t = \frac{\omega}{c}\sqrt{\varepsilon_2(\omega)} \tag{2.3}$$

This equation is the dispersion relation for coupled modes arising from interactions between light and substrate excitations. Such excitations are called polaritons and they can propagate in the metal provided $\varepsilon_2(\omega) > 0$. The quantity $\varepsilon_2(\omega)$ may be negative in a given frequency range, preventing the existence of polaritons in the metal. There is however a similar coupled mode that can propagate along the metal surface and it corresponds to the surface polaritons (SPs). The dispersion relation for such SPs can be derived and found to be:

$$q = \frac{\omega}{c}\sqrt{\frac{\varepsilon_2\varepsilon_1}{\varepsilon_2 + \varepsilon_1}} \tag{2.4}$$

where q = modulus of SP wave vector.

For such SPs to exist, the following condition should be met beside the fact that $\varepsilon_2(\omega) < 0$.

$$\varepsilon_2(\omega) < -\varepsilon_1 \tag{2.5}$$

For a Drude model, it can be shown that:

$$\varepsilon_2(\omega) = 1 - \frac{\omega^2_p}{\omega_s} \tag{2.6}$$

$$\omega_s = \frac{\omega_p}{\sqrt{2}} \tag{2.7}$$

where ω_p = bulk plasmon frequency and ω_s = surface plasmon frequency.

Equation (2.4) shows that q is always greater than $\frac{\omega}{c}\sqrt{\varepsilon_1}$ while the wave vector component of the traveling light wave in medium 1 parallel to the surface, k_x, is less than this value. Therefore q and k_x at all incident angles of light cannot match each other.

SPs are thus non-radiative modes and cannot be excited by incident light at a flat interface between a dielectric and a metallic medium. There are however ways to circumvent this difficulty and provide a means to excite SPs. They are summarized as follows.

1. Otto configuration
2. Kretschmann configuration
3. Metalic diffraction grating
4. Dielectric particles on a metallic surface

2.2.1 Otto Configuration

One way to "enlarge" the light wave vector is to shine it on a prism with a

refractive index $n > \sqrt{\varepsilon_1}$ in the so-called Otto configuration (Figure 2.1).

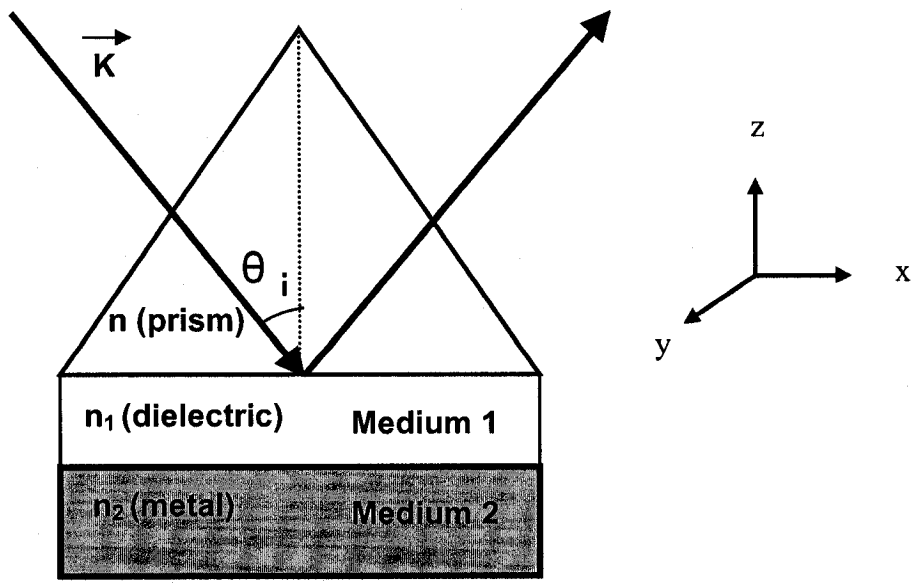

Figure 2.1 *Otto Configuration*

The component of the wave vector parallel to the surface, k_x in three different media (prism, dielectric, and metal) is the same and equal to $\frac{\omega}{c} n \sin\theta_i$ where θ_i is the incident light angle. If k_x is equal to q and greater than $\frac{\omega}{c}\sqrt{\varepsilon_1}$, excitation of SPs will be possible. Moreover, the condition for total internal reflection at the prism/medium1 interface should be satisfied, i.e.:

$\theta_i > \arcsin\frac{\sqrt{\varepsilon_1}}{n}$. The overall condition for SP excitation can be expressed as follows [10]:

$$n\sin\theta_i = \sqrt{\frac{\varepsilon_2(\omega)\varepsilon_1}{\varepsilon_2(\omega)+\varepsilon_1}} \qquad (2.8)$$

2.2.2 Kretschmann Configuration

This method is similar to the Otto one, except that in this case the metal is deposited on the prism and its thickness should be less than a few 100 Å, which is less than the evanescence wave penetration depth [11].

2.2.3 Metallic Diffraction Grating

A diffraction grating is an optical device with thousands of narrow, closely spaced parallel grooves (slits). When a beam of light is incident at angle θ_i on the surface of a grating, it is diffracted at the angle of θ_m. The grating equation is obtained as the following [12], [13]:

$$d (\sin \theta_i - \sin \theta_m) = \pm m\lambda \qquad (2.9)$$

where

d = the distance between two adjacent slits

m = an integer

λ = the wavelength of light

Since $k = \frac{2\pi}{\lambda} = \frac{\omega}{c}$, equation (2.9) can be reformulated as:

$$k_{mx} = k_{ix} \pm 2\pi \frac{m}{d} \qquad (2.10)$$

where

k_{ix} = modulus of wave vector of incident light in the grating plane

k_{mx} = modulus of wave vector of diffracted light in the grating plane

Matching the light with the SP wave, the following condition should be considered:

$$\frac{\omega}{c}\sqrt{\varepsilon_1}\sin\theta_i \pm 2\pi\frac{m}{d} = q \qquad (2.11)$$

2.2.4 Dielectric Particles on a Metallic Surface

In this method SPs wave can be excited by coupling of light with the transparent dielectric particles deposited on a metallic surface. This can be achieved via the mirror-image effect. A reflectance drop at the resonance frequency dielectric is observed by this method [4].

The transparent dielectric materials can be in the form of a granular film that is described in the static dipole approximation and considered to have an effective optical thickness and an effective dielectric constant. Moreover the particles forming the granular film can be described as having a spheroidal shape with a circular cross section parallel to the substrate. In order to use the dipole approximation, the particle size should be very small as compared to the incident light wavelength. With the above assumptions, the effective depolarization factors for the dielectric particles, $F_{\|}$ and $F_{\perp}$, are as follows:

$$F_{\|} = f_{\|} - \left(\frac{\gamma^2}{24\eta^3}\right)\left(\frac{\varepsilon_s - 1}{\varepsilon_s + 1}\right) - \frac{1.432\, d_w}{2a(\varepsilon_s + 1)} \tag{2.12}$$

$$F_{\perp} = f_{\perp} - \left(\frac{\gamma^2}{24\eta^3}\right)\left(\frac{\varepsilon_s - 1}{\varepsilon_s + 1}\right) - \frac{1.432\, \varepsilon_s d_w}{a(\varepsilon_s + 1)} \tag{2.13}$$

where the directions $\|$ and $\perp$ refer to the film plane and

γ = the axial ratio or the ratio between the axis parallel and perpendicular to the film surface plane

η = distance between the induced dipole and its mirror image divided by the rotational axis of the ellipsoid

d_w = the film mass thickness

a= inter particle distance

ε_s = the dielectric constant of the metal

$f_{\parallel}$ and $f_{\perp}$ = the real depolarization factors of the spheroidal particles

In the above equations, the second term shows the interaction between the induced dipole and its mirror image in the substrate and the third one shows their interaction with the surrounding area.

Furthermore, the effective dielectric constant components of the granular film are obtained by:

$$\varepsilon_{\parallel} = 1 + \frac{Q}{F_{\parallel} + G} \tag{2.14}$$

$$\varepsilon_{\perp} = \left(1 - \frac{Q}{F_{\perp} + G}\right)^{-1} \tag{2.15}$$

where

Q= filling factor of the dielectric particles and

$$G = \frac{1}{(\varepsilon_i - 1)} \tag{2.16}$$

with ε_i = the intrinsic dielectric constant of the particles

As in other methods, with a consideration of a free-electron metal for the substrate described by the Drude formulation, expressions for resonance frequencies can be derived [4]:

$$\omega_{\parallel} \approx \omega_s \sqrt{\frac{f_{\parallel} - A + G}{f_{\parallel} + G - \frac{B}{4}}} \tag{2.17}$$

$$\omega_{\perp} \approx \omega_s \sqrt{\frac{f_{\perp} - 2A + B + G}{f_{\perp} + G + \frac{B}{2}}} \tag{2.18}$$

where

$A = \frac{\gamma^2}{24\eta^3}$, $B = \frac{1.432\, d_w}{a}$ and ω_s is the surface plasmon frequency of the metal.

In order to calculate the reflectivity of a metallic surface overcoated with a layer of dielectric particles described earlier, the following equations are used. If $n_{\|} = (\varepsilon_{\|})^{1/2}$, $n_{\perp} = (\varepsilon_{\perp})^{1/2}$, and $n_s = (\varepsilon_s)^{1/2}$, the reflectivity coefficients for p- and s-polarized light (R_p and R_s respectively) at the incident angle θ_0 are given by [6]:

$$Rp = \frac{r_{1p} + r_{2p}\, e^{-j2\beta_p}}{1 + r_{1p}\, r_{2p}\, e^{-j2\beta_p}} \tag{2.19}$$

$$Rs = \frac{r_{1s} + r_{2s}\, e^{-j2\beta_s}}{1 + r_{1s}\, r_{2s}\, e^{-j2\beta_s}} \tag{2.20}$$

$$r_{1p} = \frac{n_{\|}\, n_{\perp} \cos\theta_0 - (n_{\perp}^2 - \sin^2\theta_0)^{1/2}}{n_{\|}\, n_{\perp} \cos\theta_0 + (n_{\perp}^2 - \sin^2\theta_0)^{1/2}} \tag{2.21}$$

$$r_{2p} = \frac{-n_{\|}\, n_{\perp} \cos\theta_0 + n_s (n_{\perp}^2 - n_s^2 \sin^2\theta_0)^{1/2}}{n_{\|}\, n_{\perp} \cos\theta_0 + n_s (n_{\perp}^2 - n_s^2 \sin^2\theta_0)^{1/2}} \tag{2.22}$$

$$\beta_p = 2\pi \frac{d}{\lambda} \frac{n_{\|}}{n_{\perp}} (n_{\perp}^2 - \sin^2\theta_0)^{1/2} \tag{2.23}$$

$$r_{1s} = \frac{\cos\theta_0 - (n_{\|}^2 - \sin^2\theta_0)^{1/2}}{\cos\theta_0 + (n_{\|}^2 - \sin^2\theta_0)^{1/2}} \tag{2.24}$$

$$r_{2s} = \frac{-n_s \cos\theta_s + (n_{\|}^2 - n_s^2 \sin^2\theta_s)^{1/2}}{n_s \cos\theta_s + (n_{\|}^2 - n_s^2 \sin^2\theta_s)^{1/2}} \tag{2.25}$$

$$\beta_s = 2\pi \frac{d}{\lambda} (n_{\|}^2 - \sin^2\theta_0)^{1/2} \tag{2.26}$$

In the above formula, the convention defining the imaginary part of the dielectric constant as negative is considered and the angle θ_0 and θ_s are related through the following equation:

$$n_s \sin\theta_s = \sin\theta_0 \tag{2.27}$$

Chapter 3: Characterization Methods and Measurements

3.1 Atomic Force Microscopy

Atomic force microscopy was first mentioned in 1986 by Binning, Quate, and Gerber [14]. This instrument utilizes a sharp probe moving over the sample. The probe is ended by a tiny tip located on the end of the cantilever. Most AFM instruments use an optical lever technique. Figures 3.1 and 3.2 illustrate how this technique is working.

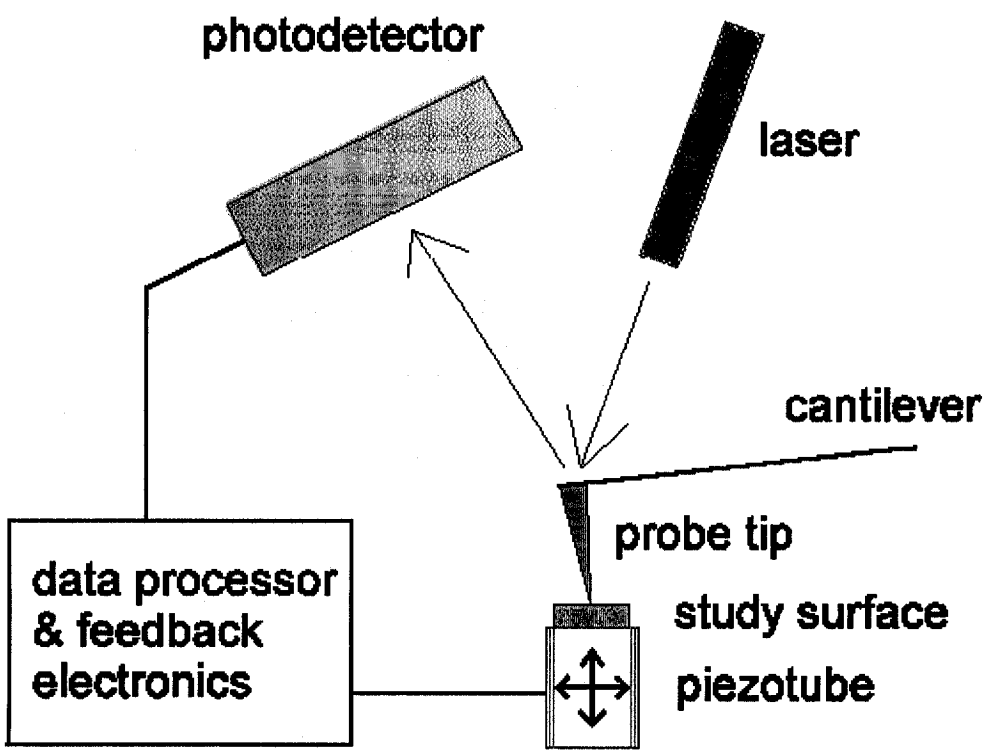

Figure 3.1 *The schematic illustration of the AFM system [15]*

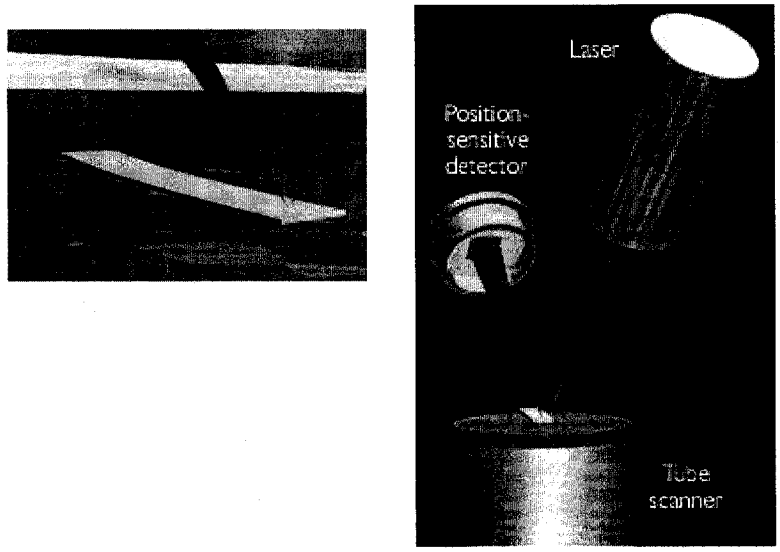

Figure 3.2 *Concept of AFM and the optical lever: (left) a cantilever touching a sample; (right) the optical lever [16]*

The reflected laser beam is detected by a sensitive photocell. By measuring different signals, the bending of the cantilever can be measured. The movement of the tip can be performed by a device made from piezo-electric ceramics in the form of a tube scanner. This scanner controls the movement of the tip or samples in the x, y, and z directions. The range of this movement is around 90 μm in the x and y directions, and 5 μm in the z direction.

3.1.1 Modes of Operation

There are three main modes of operation:

1. Contact mode
   - Constant force or constant distance (strong repulsive force)
2. Tapping mode
   - Constant force or constant distance (weak force)
3. Non-contact mode

3.1.2 Contact Mode

In the contact mode the tip scans the surface of specimen while monitoring the change in cantilever deflection with a split photodiode detector. Here the tip contacts the surface through the adsorbed fluid layer on the sample surface and a feedback loop collects a constant deflection between the cantilever and the sample by vertically moving the scanner at each (x,y) data point to maintain a setpoint deflection. Then with a constant cantilever deflection, the force between the tip and the sample remains constant. This force is calculated from Hooke's Law:

$$F = -(K)(x) \tag{3.1}$$

where F = force, K = spring constant, and x = cantilever deflection. Finally by storing the vertical distance at each (x,y) in the computer the surface image is obtained. Although this method cannot be used for soft samples, it has the following advantages:

1. High resolution, 1.5 nm laterally and 0.015 nm vertically.
2. Operation in air and aquatic environments.
3. High scan speeds.

3.1.3 Tapping Mode

The tip still contacts the surface but with a weaker force applied, so this method is useful for soft surfaces. The cantilever is oscillated at almost its resonance frequency with an amplitude between 20 nm and 100 nm. The tip taps on the sample surface. Then the feedback loop collects the constant oscillation amplitude by maintaining a constant RMS of the oscillation signal acquired by the split photodiode detector. Finally by saving the vertical position of the scanner at

every (x,y) and finding a setpoint for that, a form of image topography is obtained.

This method can be less damaging to soft surfaces and it has the advantage of identification of surface containments which are not seen by the Non-Contact method.

3.1.4 Non-Contact Mode

The cantilever is oscillated at a frequency which is slightly above the cantilever's resonance frequency with an amplitude less than10nm to obtain an AC signal from the cantilever. In this method the tip does not contact the sample surface; however it oscillates above the surface near the adsorbed fluid layer. Then a feedback loop collects a constant oscillation amplitude or frequency by vertically moving the scanner at every (x,y) data point until a "set point" amplitude or frequency is reached. The distance at every (x,y) is stored by computer to make a topographic image. The advantage of this method lies in the avoiding of an applied force on the surface of samples, but the image resolution and the scanning speed are less attractive than in the previous modes.

3.1.5 AFM Measurements

The AFM images were obtained from a Multi Mode AFM model MM AFM-2, using Scanner As-130 (J) with a maximum scan size area of 125 x 125 μm and a vertical size of 5.0 μm in the tapping mode. The tip material was made of antimony (n) doped Si which functions at resonance frequency f_0 = 110~ 140 KHz with force constant K =20~80 N/m and dimensions: t= 3.5~ 4.5 μm, w= 25~ 35 μm, and L= 110~ 140 μm, where the t, w, and L are the thickness, the width, and

the length of the cantilever, respectively. Figure 3.3 shows a photograph of the instrument used:

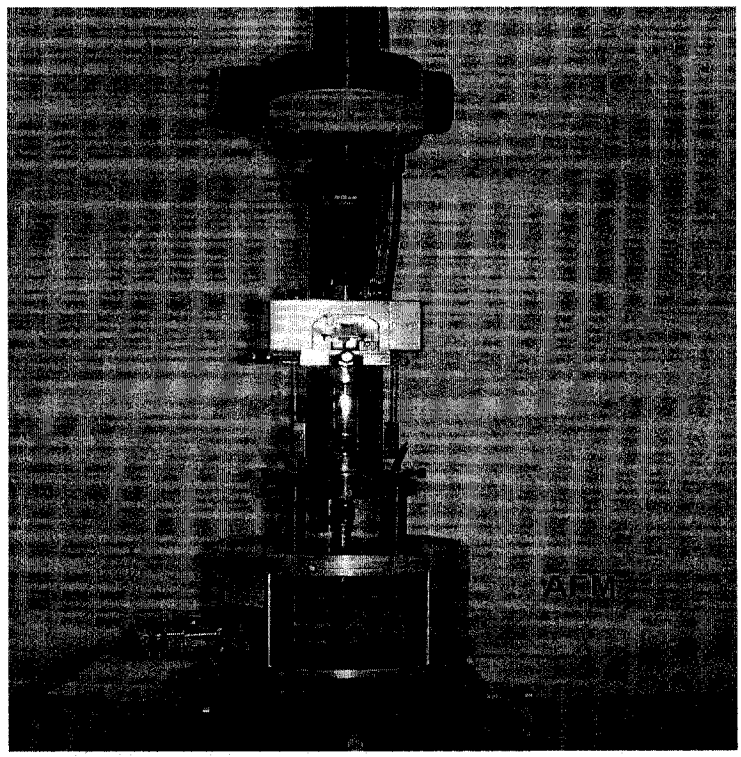

Figure 3.3 *MM AFM-2 with Scanner As-130 (J)*

3.2 X-ray Diffraction (XRD)

X-ray diffraction (XRD) is a powerful non-destructive technique for characterizing crystalline materials. It provides information on structures, phases, preferred crystal orientations (texture) and other structural parameters such as average grain size, crystallinity, strain and crystal defects [17]. X-ray diffraction peaks are produced by constructive interference of monochromatic beam scattered from each set of lattice planes at specific angles. The peak intensities

are determined by the atomic decoration within the lattice planes. Consequently, the X-ray diffraction pattern is the fingerprint of periodic atomic arrangements in a given material. An on-line search of a standard database for X-ray powder diffraction pattern enables quick phase identification for a large variety of crystalline samples.

Specular X-ray reflectivity (XRR), a technique parallel to X-ray diffraction, is now becoming a widely used tool for the characterization of thin-film and multilayer structures. X-ray scattering at very small diffraction angles allows characterization of electron density profiles of thin film down to a few tens of angstroms. Using a simulation or the least-squared fit of the reflectivity pattern, one can obtain accurate measurements of thickness, interface roughness and layer density for either crystalline or amorphous thin films or multilayer. The following figure shows the schematic of XRD system:

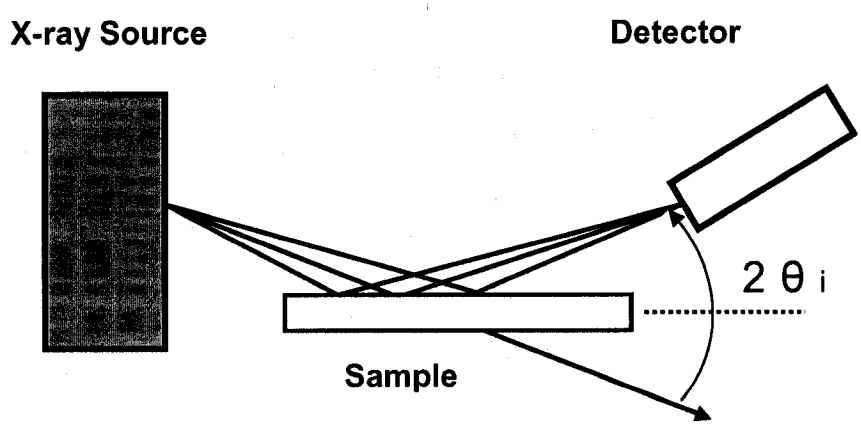

Figure 3.4 *The schematic illustration of XRD system*

This method has the following applications:

1. Determination of phase contents of reaction products

2. Measurement of average crystallite size, strain or micro-strain effects in bulk and thin-film samples.
3. Quantification of preferred orientation (texture) in thin films and multi-layers.
4. Refinement of lattice parameters
5. Determination of thickness, interface roughness and density for thin films and multi-layers.

A typical diffractometer consists of a source of radiation, a monochromator to choose the wavelength, slits to adjust the shape of the beam, a sample and a detector. In a more sophisticated apparatus, a goniometer can be used for fine adjustment of the sample and the detector positions. When an area detector is used to monitor the diffracted radiation, a beamstop is usually needed to stop the intense primary beam that has not been diffracted by the sample. Otherwise the detector might be damaged. Usually the beamstop can be completely impenetrable to the x rays or it may be semitransparent. The use of semitransparent beamstop allows the possibility to determine how much the sample absorbs the radiation using the intensity observed through the beamstop.

X-ray diffraction patterns of the films on their substrates were obtained in reflection mode using a custom-built theta-theta diffractometer. The instrument is equipped with a pyrolytic graphite monochromator and analyzer crystals. The data are displayed as a function of $q = 4\pi \sin(\theta)/\lambda$, where λ is the wavelength of the Cu-K alpha radiation used in the experiment ($\lambda = 0.154178$ nm) and 2θ is the scattering angle. In addition to longitudinal θ-2θ scans, rocking curves were measured at constant 2θ in order to determine the range of gold grain

orientations relative to the Si (111) substrate. Figure 3.5 depicts the instrument that was used for measurements in this experiment.

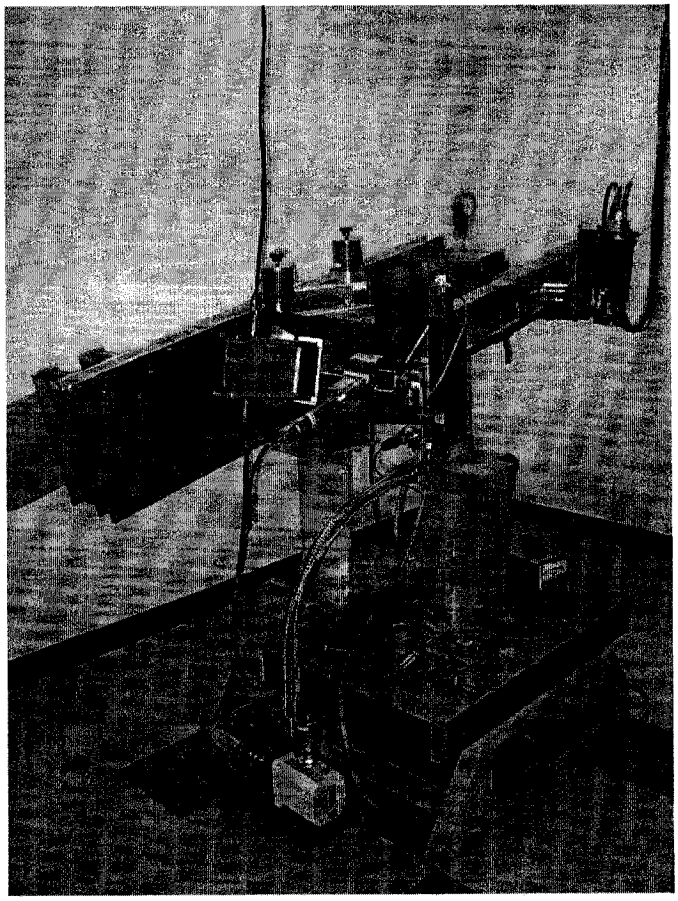

Figure 3.5 *The custom-built theta-theta diffractometer*

3.3 Fourier Transform Infrared (FTIR) Spectroscopy

Infrared spectroscopies are analytical methods that measure the infrared intensity versus the wavenumber or the wavelength of light, and can be utilized in the far or mid-infrared range. These kinds of spectroscopy detect the vibration characteristics of chemical functional groups in a sample. When an infrared light

is incident on the material, the chemical bonds will bend, contract, and stretch. Thereby, regardless of the structure of the rest molecule, in a specific wavenumber range the functional group absorbs the infrared radiation by which it can be identified.

The early-stage IR apparatus uses a prism or grating monochromator and was a slow characteristic scanning, but the fourier transform infrared (FTIR) spectrometer obtains the spectra by collecting an interferogram of a sample signal with an interferometer, which measures all of infrared frequencies [18]. Figure 3.6 shows the schematic illustration of a FTIR system.

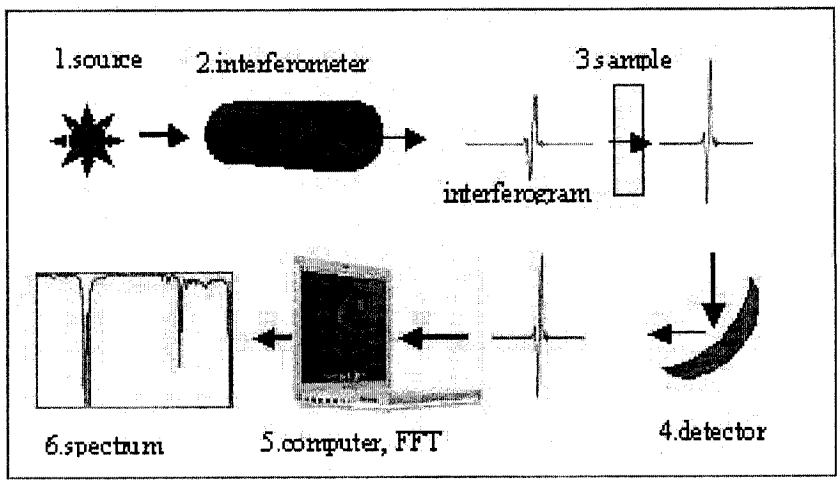

Figure3.6 *Schematic illustration of a FTIR system [19]*

In this system, the IR beam is splitted into two beams by a beamsplitter located in the interferometer. One beam reflects from a fixed mirror and the second one from a moving mirror. Then they are combined in beamsplitter

undergoing the interference. This signal is called interferogram and contains all frequencies of the IR beam encoded into it. When this signal is reflected or transmitted from the sample, some frequencies of energy are adsorbed by the sample due to the excited vibration of functional groups in molecules. Finally the beam arrives at the detector, but because it cannot be directly interpreted and has to be decoded, a computer performs the FT calculation, and presents an infrared spectrum by plotting the absorbance or transmittance versus wavenumber.

If a spectrum, obtained without the sample (background spectrum), has characteristics bands around 3500 cm^{-1} and 1630 cm^{-1}, it describes the atmospheric water vapor while its bands at 2350 cm^{-1} and 667 cm^{-1} are attributed to carbon dioxide. This background spectrum should always be run during the sample analysis. The spectrum obtained with samples looks like the background one except that the sample peaks are superposed upon the instrumental and atmospheric contributions to the spectrum [20].

For eliminating these contributions, the spectrum can be normalized by the following equation:

$$\%T = I / I_0 \tag{3.2}$$

where %T is the transmittance, I is the intensity with a sample, and I_0 is the intensity of background. The absorbance A can be calculated from the following equation:

$$A = -\log_{10}(T) \tag{3.3}$$

The FTIR used in this experiment was a NEXUS 870 FT-IR with a laser with wavenumbers ranging from 400 to 4000 cm^{-1}.

3.4 Raman Spectroscopy

The main spectroscopes used to find the vibrations in molecules are based on processes of infrared absorption and Raman scattering. They are broadly used to show the chemical or physical structures. They identify the materials and their quantities from their fingerprint or spectral patterns. The measurements can be done with samples in different phases, sizes, temperatures, and even on different surface layers.

Raman spectroscopy, unlike infrared spectroscopy, applied a single frequency of radiation incident on the sample. Here the light interacts with molecules, polarizes a cloud of electrons around the nuclei and forms a virtual state or short-lived state. If the incident and scattered light have almost the same frequency or the same energy, it will be called elastic scattering or Rayleigh scattering. In this case the electron is directly excited from the ground state to the vibrational state. On the other hand, if the nucleus is induced, the energy will transfer from the photon to the molecule or vice versa. In this case, the scattering is inelastic and the photon energy or frequency is changed. This phenomenon is called Raman scattering [21], [22].

Since only one in 10^6-10^8 photons which scatter is from Raman scattering, a modern laser and microscope is used to carry high density measurements. Figure 3.7 depicts the Rayleigh and Raman scattering processes. The Rayleigh process will happen when a molecule is excited and then return to the same energy- state. Consequently the frequency and energy remain constant.
On the other hand, the Raman scattering will happen when a molecule is excited to a higher vibrational state by absorption of light (Stokes scattering).

However, because of thermal energy, some molecules present are in an excited state. They can be brought to a lower energy state (ground state) and are called anti-Stokes scattering.

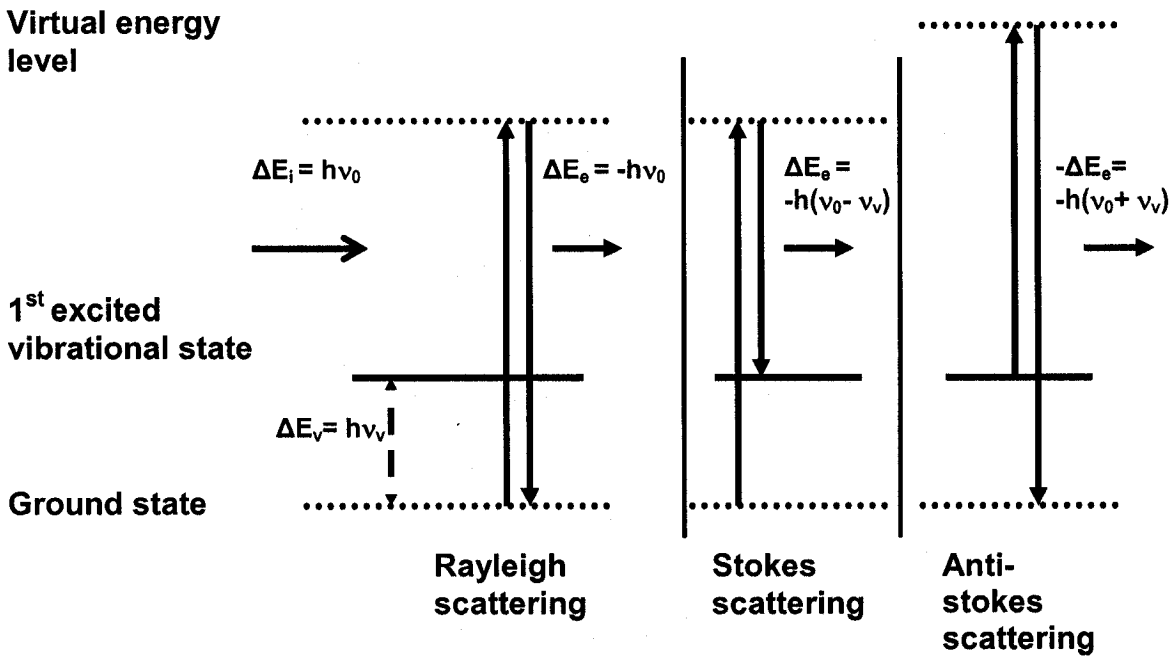

Figure 3.7 *The different possibilities of visual light scattering: Rayleigh scattering (no Raman effect), Stokes scattering (molecule absorbs energy) and anti-Stokes scattering (molecule loses energy)*

3.4.1 Micro Raman Spectra Measurements

The apparatus used to record the Raman spectra was a Labran HR with a Raman-IR microanalytical spectrometer equipped with the following:

1. A 17 mW He-Ne laser emitting at 632.8 nm
2. A holographic notch filter (Kaiser Optical System, Model: Super Notch-Plus)

3. A 256 x 1024- pixel CCD detector
4. A computer- controlled XY stage with a spatial resolution of 0.1 µm
5. Two interchangeable gratings (950 and 1800 mm^{-1}, respectively)
6. A confocal microscope with 10, 50 and 100 x objectives with a lateral spatial resolution of approximately 10, 2 and 1 µm, respectively

The laser power was 9 mW on the sample surface and the spectral resolution is less than 0.5 cm^{-1} for a slit width of 150 µm and a confocal hole of 300 µm. Micrometric imaging has been performed, two samples areas of respectively 25 x 25 µm and 10 x 10 µm were considered and the laser beam is scanned over it by moving the sample with the computer-controlled XY stage. Finally the divisions of the total area in cells of 3 x 3 µm and 1 x 1 µm have been chosen.

The micro-Raman analysis was performed with an HR combined Raman-IR micro analytical apparatus, equipped with a motorized xy stage and auto focus. The spectra were generated with 632.8 nm He-Ne laser excitation. The power of the laser out of the objective, a 100 x with numerical aperture (NA) of 0.90, was about 9 mW, and the focused laser spot had a 1 µm diameter. The spectral resolution of this apparatus is estimated to be around 0.5 cm^{-1} for a slit width of 150 µm and a confocal hole of 300 µm. Two different acquisition modes were used. The first was the single point acquisition while in the second acquisition mode, an area is defined on the sample and the laser beam is scanned over it by moving the sample with the computer-controlled XY stage. In this study, a division of the total area in cells has been chosen. Figure 3.8 shows the apparatus which was used in this study.

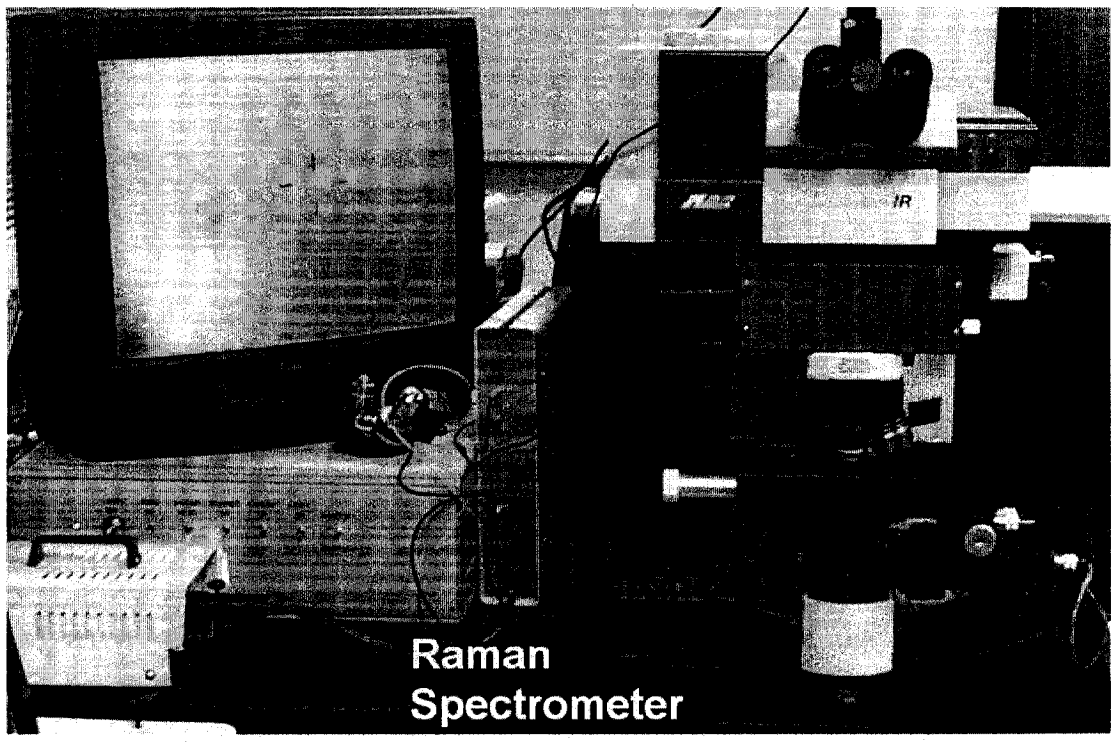

Figure 3.8 *Labran HR with Raman-IR microanalytical spectrometer*

3.5 Spectrophotometer

A spectrophotometer can produce light at a selected wavelength besides being a photometer that can measure light intensity as a function of the wavelength of light. Important features of spectrophotometers include the type of light sources, the measurement technique, the spectral bandwidth and the linear range. The most common application of spectrophotometers is the measurement of light absorption, but they can also be designed to measure diffuse or specular reflectance [23].

There are two major classes of spectrophotometers; single beam and double beam. A double beam spectrophotometer measures the ratio of the light intensity on two different light paths, and a single beam spectrophotometer measures the absolute light intensity. Although ratio measurements are easier, and generally stabler, single beam instruments have some advantages; for instance, they can have a larger dynamic range.

The spectrometer used in our experiments operated in the ultraviolet, visible and near infrared range. All the reflection spectra were measured on a Cary 5000 double beam spectrophotometer using a near-normal incidence (8°) specular reflection attachment and the measurements were made relative to a reference mirror. In this experiment the smallest surface area without using a mask was12mm and 2mm with a mask.

Chapter 4: Sample Preparation

4.1 Deposition of a Silver or Gold Film by Sputtering

Sputtering is a process used to deposit a thin film onto a substrate in a vacuum ambient. In this process, a high voltage is applied across a low pressure gas to create a plasma consisting of electrons and ions in a high energy state. The gas used in the sputtering process can be argon gas. In such case, the argon ions hit the metallic target which is connected to a negative voltage and works as a cathode. This collision provokes the removal of the metal atoms from the target. The metal atoms move towards the substrate which is located at the anode and a metallic film is formed on the surface of the substrate. To increase the ionization rate in this process, a magnetic ring located under the target can be used.

A dc or rf voltage can be applied in the sputtering process, the dc voltage being used when the target is conducting. When the target is non-conducting, surface charging resulting from positive ions bombardment can shield the electric field and stop the process. In such case, an rf voltage used.

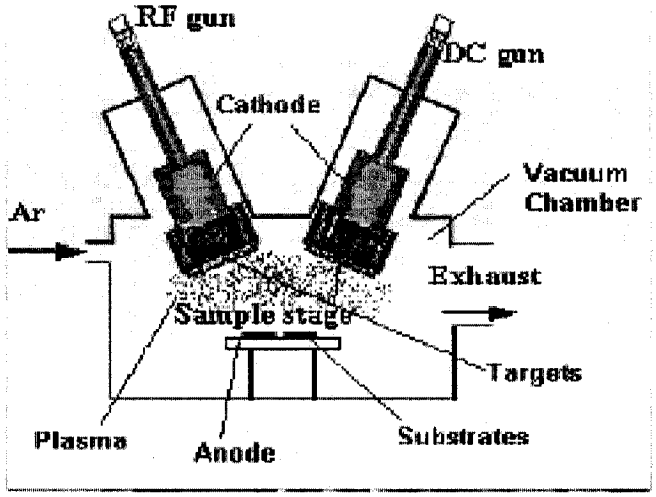

Figure 4.1 *The schematic illustration of a dc and rf sputtering machine [24]*

In the dc-magnetron sputtering method used in our experiments, the deposited film properties can be controlled by parameters such as the applied voltage, the gas flow rate, the applied current, and the vacuum pressure. The applied voltage determines the adequate energy to release the sputtered particles from target and also provides a sputter yield that sets the number of deposited particles per incoming ion. The gas flow rate regulates the ions striking the metal surface. The applied current determines mainly the rate of deposition and thereby the time of arrival of the particles on the substrate during the growth process. Finally the pressure in the sputter chamber controls the collisions of particles on their way from the target to the substrate. The dc-magnetron sputtering machine used was a MagSput-2G2 machine with an Alcatel 2012-A mechanical pump, a Turbovac 151 turbomolecular pump, a chiller, and a sputtering target of pure silver or gold (99.999% purity, 3 mm thickness and 2"

diameter). The substrate (glass or silicon) is cleaned by a detergent solution in an ultrasound bath, and then rinsed in deionized water, acetone, and isopropyl alcohol. Table 4.1 shows the experimental parameters used while Figure 4.2 shows the sputtering machine used in this experiment:

Type of film	Applied voltage [V]	Argon flow rate [sccm]	Applied current [A]	Sputtering rate [Å/s]	Vacuum pressure [Torr]	Final thickness [nm]
Silver (Ag)	450	180	1.2	8.5	$3x10^{-3}$	120~170
Gold (Au)	450	100	1.2	5	$3x10^{-3}$	170,750

Table 4.1 *The experimental parameters for the deposition of Ag and Au on glass or silicon substrates*

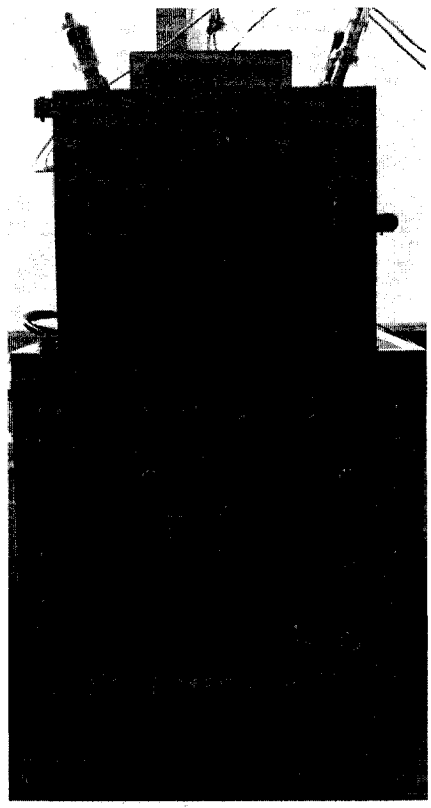

Figure 4.2 *The MagSput-2G2 puttering machine*

4.2 Fabrication Method of the Tin Dioxide (SnO_2) Film

The method used here is called the sol-gel dip coating (SGDC) method. In this technique solid materials are formed by hydrolysis and condensation reactions. The technique can be used to prepare many types of materials such as thin films of metal oxides and ceramics. In order to prepare a metal oxide by this technique, a suitable precursor or initial agent such as metal alkoxide with the general formula $M(OR)_x$ (M is a metal such as Sn, Zn, Al and R is an alkyl or related group) is dissolved in a solvent such as alcohol.

In this process four main forming steps are present: 1. the preparation of the solute, 2. the gel formation, 3. the drying, and 4. the thermal treatment. The sol-gel technique is based on the hydrolysis of metal alkoxide followed by condensation reactions of the hydrolyzed alkoxide to corresponding species. During the hydrolysis process, the alkoxide group is replaced by the hydroxo ligand as given by the following equation:

$$M(OR)_x + H_2O \rightarrow HO\text{-}\ M(OR)_{x-1} + ROH \qquad (4.1)$$

Then the hydroxo metal alkoxide starts reacting with other hydroxo or alkoxo groups either in the hydroxo metal alkoxidies or metal alkoxides. This reaction is done via condensation as the following:

$$(OH)_{x-1}M\text{-}OH + HO\text{-}\ M(OR)_{x-1} \rightarrow (OH)_{x-1}M\text{-}O\text{-}\ M(OR)_{x-1} + H_2O \qquad (4.2)$$

$$(OR)_{x-1}M\text{-}OH + RO\text{-}\ M(OR)_{x-1} \rightarrow (OR)_{x-1}M\text{-}O\text{-}\ M(OR)_{x-1} + H_2O \qquad (4.3)$$

The equation (4.2) shows the dehydrating process while the equation (4.3) shows the dealcoholation one.

Our fabrication procedure can be divided in three steps: 1) the pulling phase, 2) the drying process, and 3) the annealing stage [25].

In the first step, tin(IV)tert-butoxide was mixed with pure ethanol then stirred for one hour in diluted ethanol to obtain a 2% solution.

In the next step, a cleaned silicon substrate with sputtered gold is dipped into the solution at a speed of 12 mm/s and it remained immersed in it for 20 s. It is then pulled up at a 12 mm/s retraction speed. Depending on the desired film thickness, the dipping can be repeated after a pause of 7 min. In this work, the maximum number of dipping was 4 times. The room temperature and relative humidity were 22-24 °C and 47- 51 % respectively.

After this step, the sample is kept in the atmosphere for 24 hours in order to let the film completing the hydrolysis and condensation reactions. In the final step, the film is kept inside the oven for one hour at 500 °C. The whole process is shown in the following figure, giving us samples of useful dimensions of 3 x 0.5 cm.

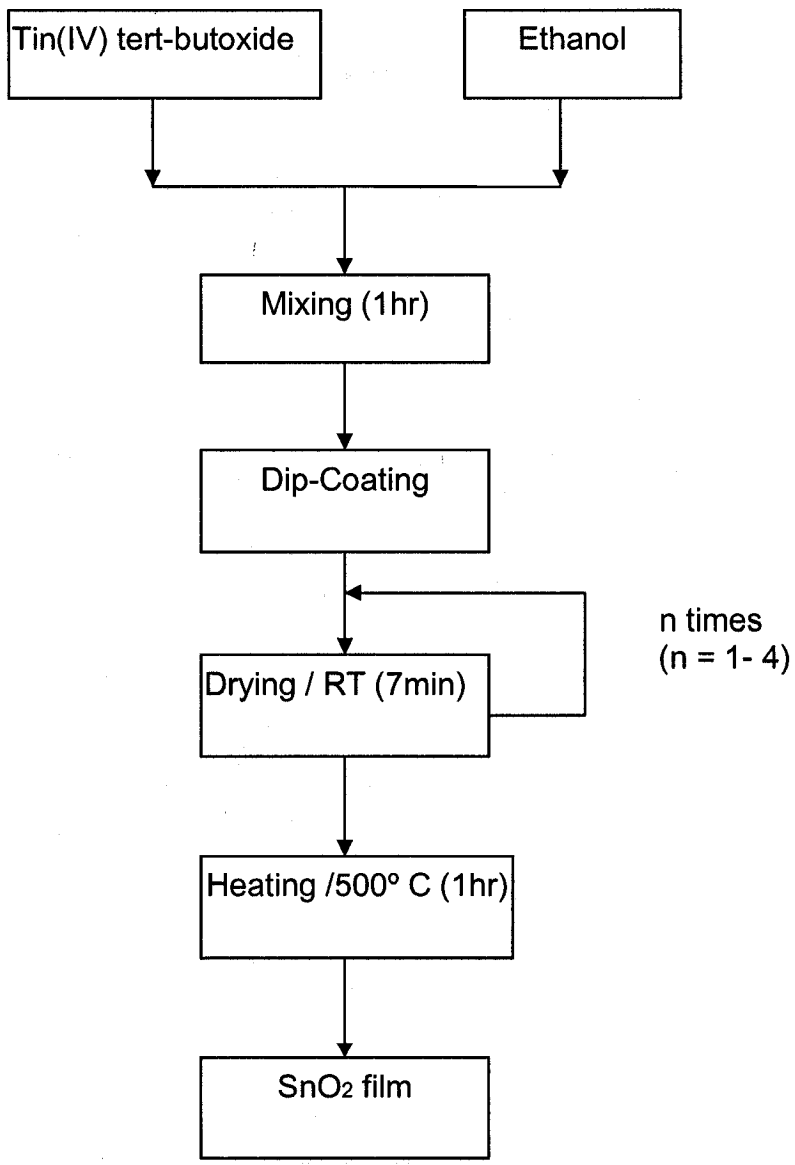

Figure 4.3 *Flow-chart for the fabrication process of tin dioxide film*

In this technique each step should be carried out in well-determined conditions. For instance, the humidity ratio during the deposition is a crucial factor that affects the morphology of the film. Also a good control during the drying step can eliminate some defects such as cracks. The annealing conditions control the atomic densification, the electrical, optical, and morphological properties of the films.

The apparatus used in this method is a computer controlled dip-coater with a software that controls all the following parameters: immersion time, depth, of immersion, immersion speed, number of immersions, pause before immersions, and sample retraction speed.

4.3 Fabrication Method of the Titanium Dioxide (TiO_2) Film

For the preparation of TiO_2 the sol-gel deposition process was used as well [26], [27]. Here the starting material was the titanium tetra-n-butoxide (TTB), ($Ti(OC_4H_9)_4$) which was mixed with ethanol (EtOH, C_2H_5OH) and stirred. Then a mixture of water, hydrochloric acid, and ethanol was added to this solution so that the hydrolysis process can occur. At the end, an organic polymer (polyethylene glycol- PEG) was added and the mixture was stirred gently for an hour. Then the solution was used to produce the TiO_2 film.

In the next step, a cleaned glass substrate with sputtered silver was immersed in the solution at the rate of 0.1 mm/s and then withdrawn at 0.4 mm/s. The film was then dried for 30 minutes at 80 °C inside the oven and immersed in boiling water for up to 3 hours. Finally, the sample was cooled to room temperature. The useful dimensions of the samples obtained were 3 x 0.5 cm. Figure 4.4 shows the flow chart of the procedure.

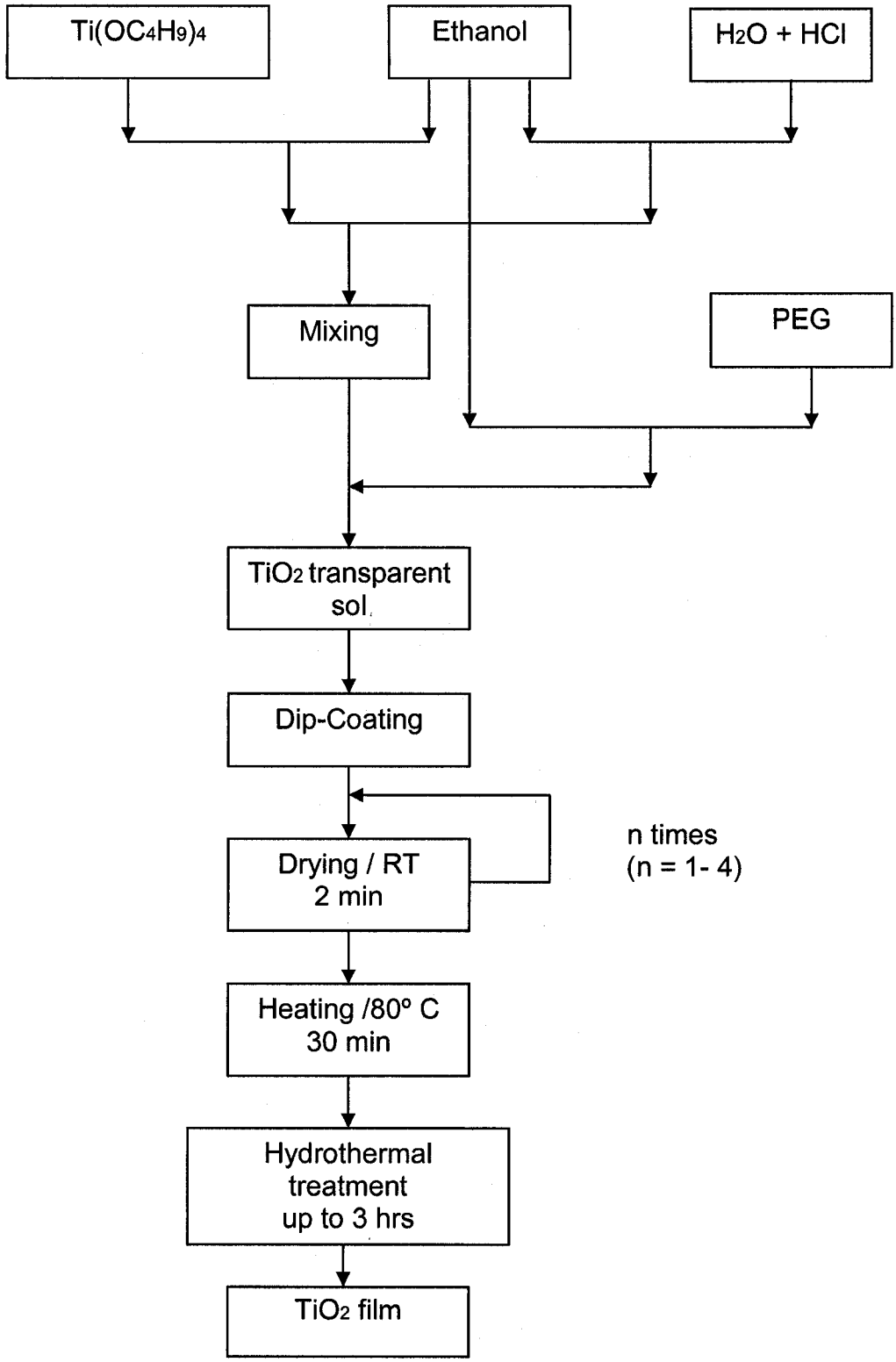

Figure 4.4 *Flow-chart for the fabrication process of titanium dioxide film*

The following figure shows the home made computer controlled dip coater which was used for the preparation of SnO_2 and TiO_2.

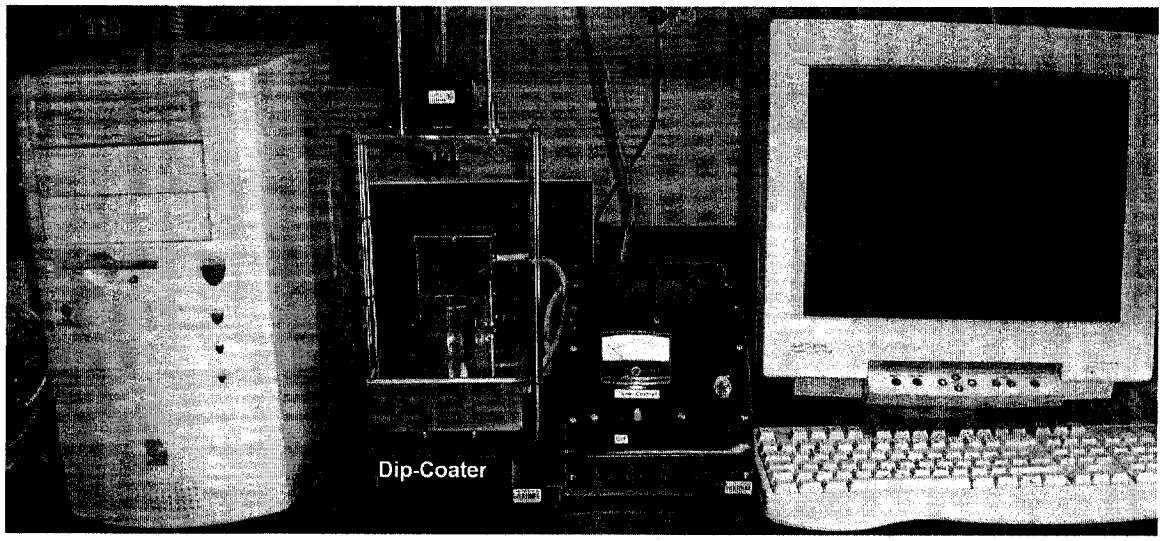

Figure 4.5 *The computer controlled dip-coater*

Chapter 5: Results and Discussion

5.1 Tin Dioxide Particles on Gold Surfaces

5.1.1 Effect of the Annealing Temperature on the Morphology and Optical Properties of the Au/SnO_2 (type A) Composite on a Glass Substrate

Figure 5.1 shows the AFM image, the surface plot and the corresponding size distribution of composites A annealed at 300, 400 and 500^{0}C, respectively. The image corresponding to the sample annealed at 300^{0}C (Figure 5.1 a) shows the presence of a majority of more or less spherical particles with a mean size of about 18 nm.

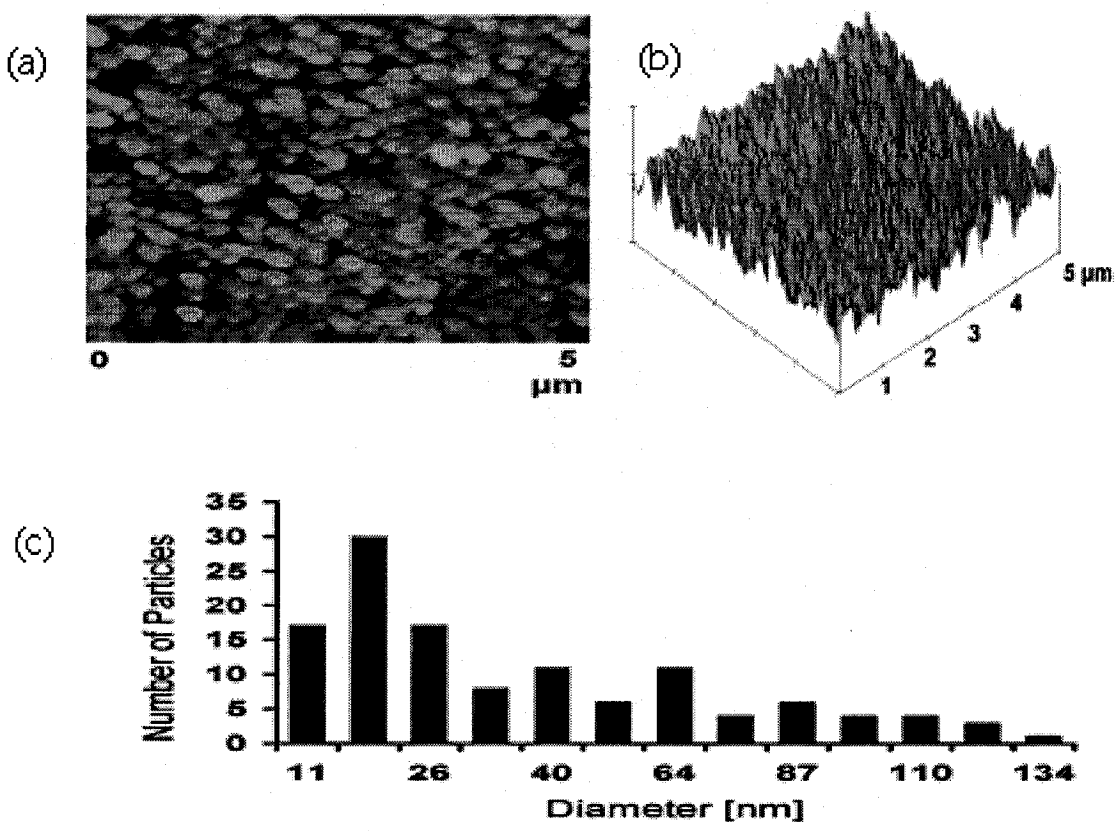

Figure 5.1 *a) The 2D, b) 3D AFM images, and c) size distribution of a Au/SnO_2 sample on a glass substrate at 300^{0}C*

As it can be seen from Figure 5.1 c, the size distribution is quite broad and a small number of larger particles are present as well. In the size distributions, both tin dioxide and Au particles are counted but tin dioxide nanoparticles are smaller than 5 nm.

Figure 5.2 clearly shows the beginning of the aggregation process in films annealed at 400^0C. It can be seen that a number of particles grow at the expense of the surrounding particles leaving empty spaces around the grown particles. The mean size of particles reaches higher values (22-40 nm) and particles as large as 180-200 nm are present in the sample.

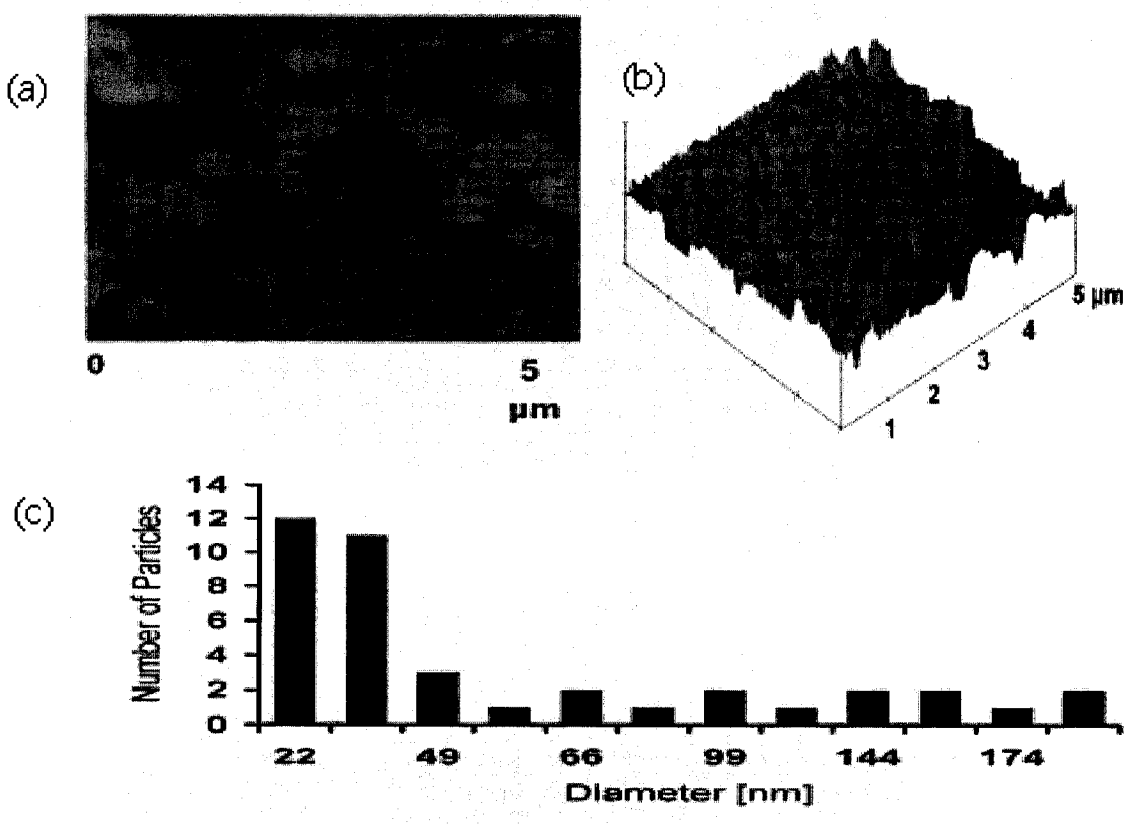

Figure 5.2 *a) The 2D, b) 3D AFM images, and c) size distribution of a Au/SnO_2 sample on a glass substrate at 400^0C*

Finally, the image shows the formation of smaller aggregates that will act as "building blocks" of the much larger aggregates seen for films annealed at 500^0C (Figure 5.3).

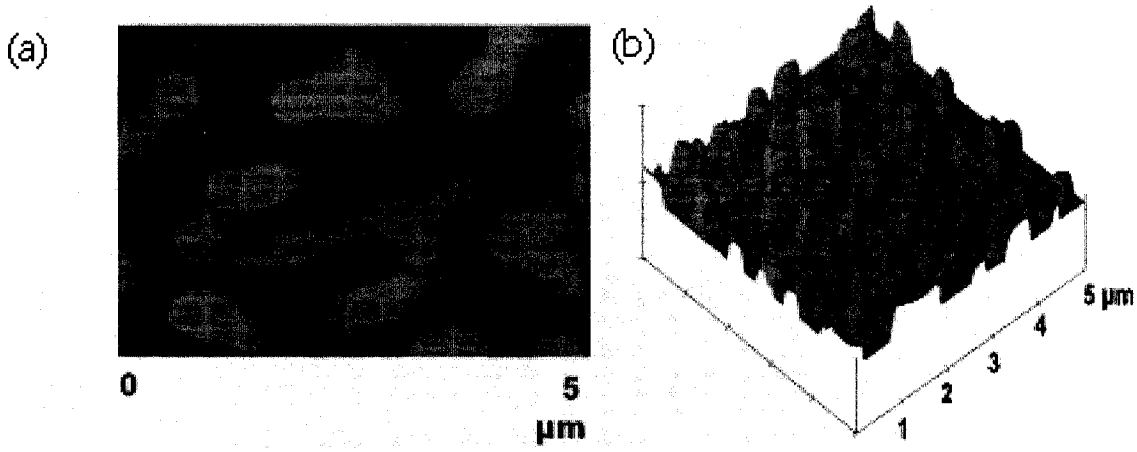

Figure 5.3 *a) The 2D and b) 3D AFM images of a Au/SnO_2 sample on a glass substrate at 500^0C*

The size of some of these large agglomerations may reach 1-2 µm and a variety of particle shapes can be seen, some similar to nanorods. The reflection curves of the samples annealed at different temperatures are given in Figure 5.4 and Figure 5.5. The optical properties, as shown by the reflection curves are in agreement with the morphology revealed by the AFM images. While there is not a marked difference between the films annealed at 300 and 400^0C, for films heated at 500^0C, the reflection curve became broad and red-shifted, clearly indicating a deviation from the spherical geometry. This behavior is in agreement with Mie theory that predicts that in this case, the transverse and longitudinal dipole polarizability no longer produce equivalent resonances. Consequently, in

addition to the transverse plasma resonance whose position remains centered around 500 nm, a broadened and red-shifted longitudinal plasma resonance will be present in the spectrum.

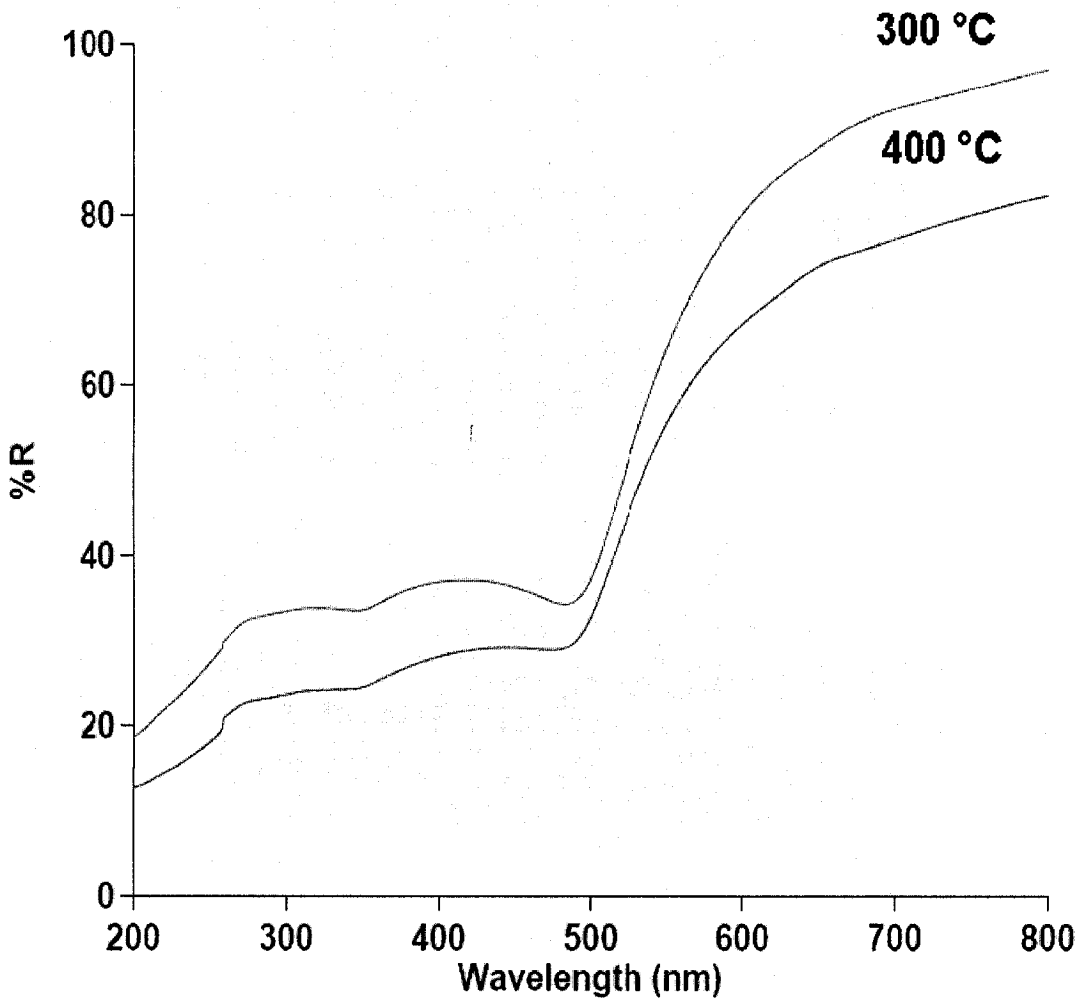

Figure 5.4 *Reflectance spectrum of a Au/SnO_2 sample on the glass at 300^{0}C and 400^{0}C*

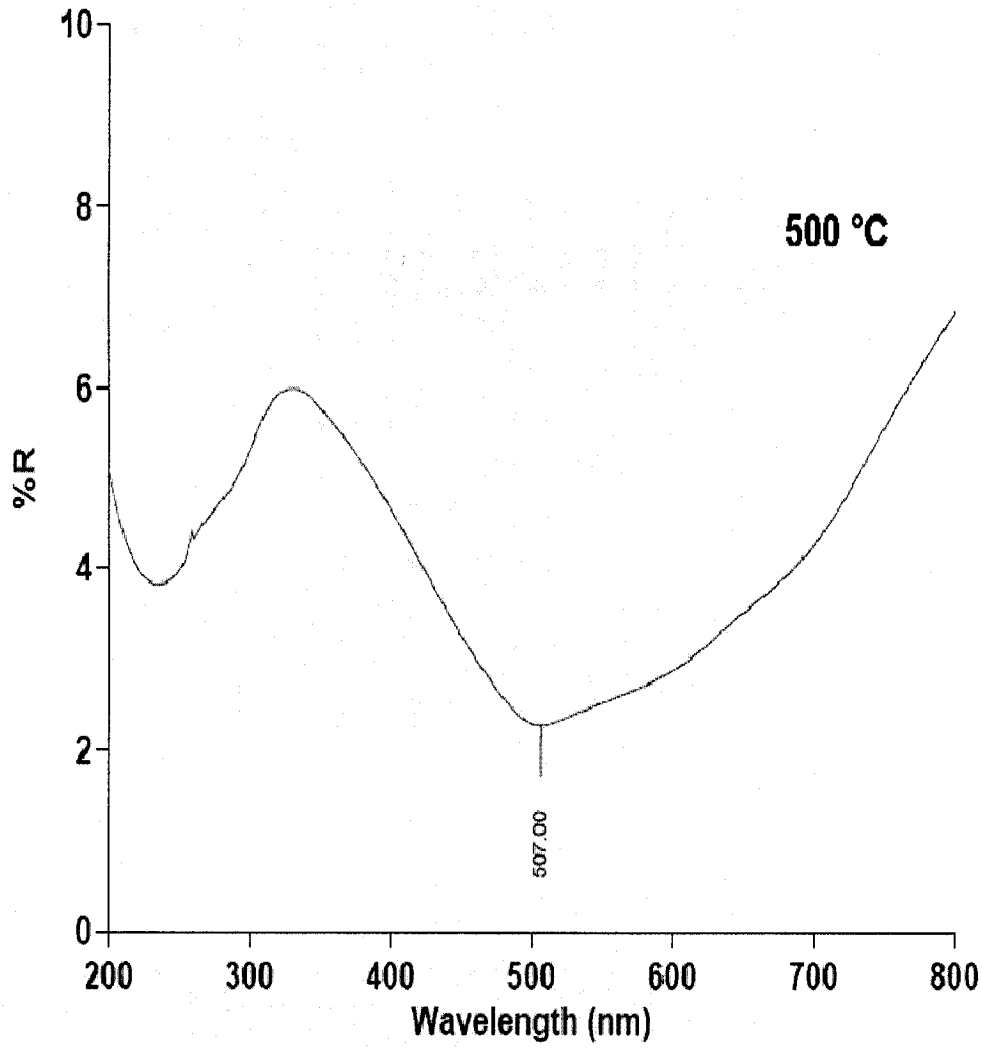

Figure 5.5 *Reflectance spectrum of a Au/SnO_2 sample on the glass at 500^{0}C*

It has been shown that aggregation causes a coupling of the gold nanoparticles plasma modes which results in a red shift and broadening of the longitudinal plasma resonance [28]. The results showed that during the annealing of thin composite films deposited on a glass substrate, there is an important change of the surface morphology and, consequently of the optical properties.

5.1.2 Effect of the Substrate and the Thickness of the Film on the Morphology of the Au/SnO_2 Composite (type B)

In order to avoid the aggregation of gold, we have prepared thicker films and used a silicon substrate instead of glass. Figure 5.6 shows the AFM images along with the corresponding particle size distribution of a representative Au/SnO_2 composite (B) film, compared to that of a pure Au film prepared and annealed under the same conditions.

The surface morphology and size distribution of the thick (750 nm) films (Figure 5.6 a and Figure 5.6 b) are compared to those found in thin (170 nm) films (Figure 5.7 a and Figure 5.7 b). It can be seen that the thick films of both Au and composite films have larger grains than the corresponding thin films. In the images of Figure 5.6, small grains appear to be connected together and elongated in one direction. As the particles of both of the materials are counted, because of the smaller size of SnO_2 nanocrystals, the mean diameter (in-plane width) of particles in the composite appears to be much lower than in the pure Au film (14 compared to 24 nm in the 750 nm film). At the same time, Figure 5.6 shows that the size distribution in the composite is narrower than in the Au film, probably, because the presence of SnO_2 within the Au particles would reduce the coalescence of the adjacent particles of gold during the annealing of the film.

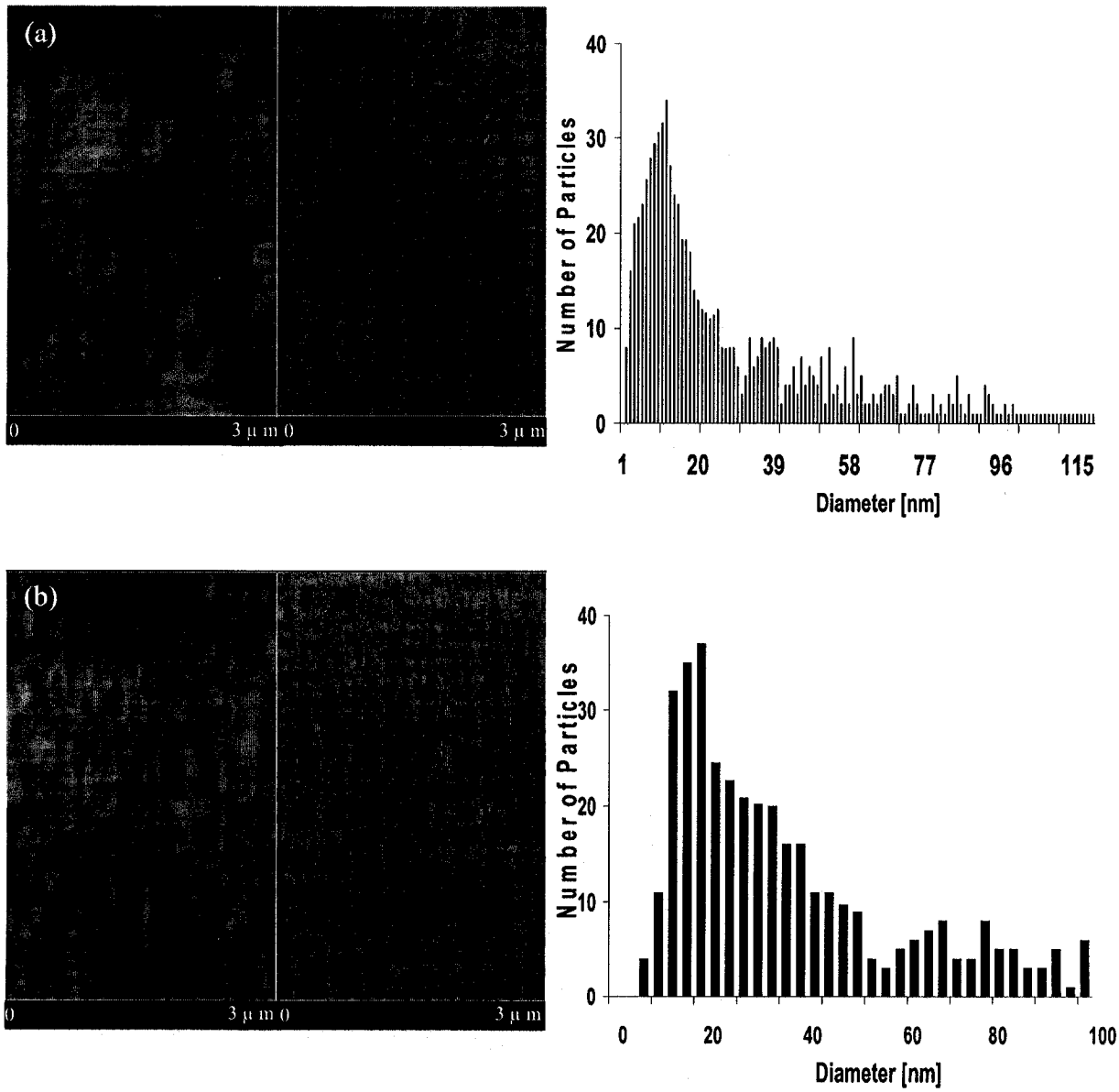

Figure 5.6 *The AFM image and size distribution of, a) Au/SnO_2 composite film b) Au film, 750 nm thick.*

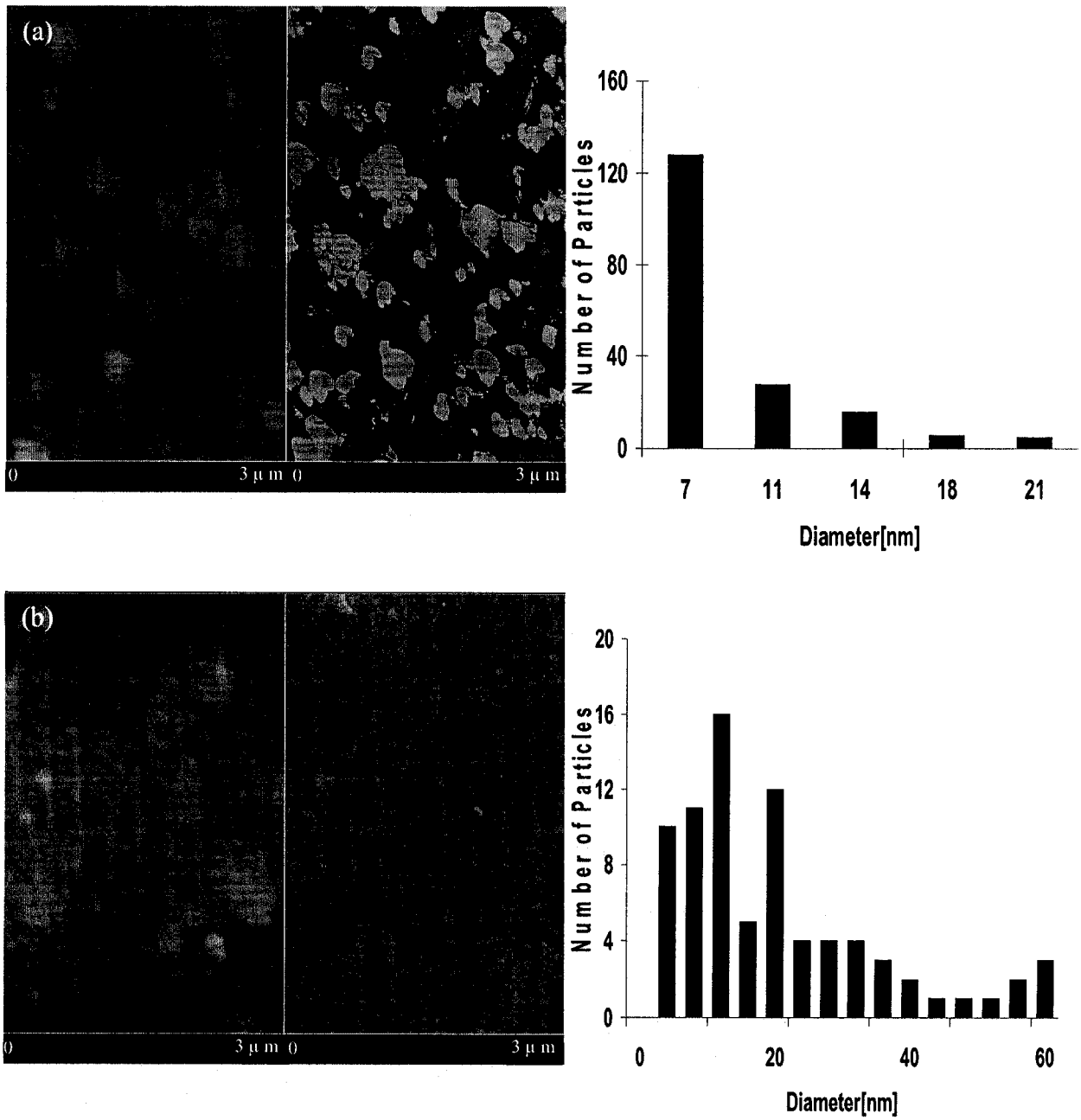

Figure 5.7 *The AFM image and size distribution of, a) Au/SnO_2 composite film b) Au film, 170 nm thick.*

The AFM images show a significant deviation from the spherical shape for all the heat-treated films but the degree of aggregation is significantly lower than in composite A. Figure 5.8 is the surface plot of the 750 nm thick composite film compared to the corresponding Au film. The presence of fairly large crystals, with some smaller particles on the non-flat top of them can be seen. Because of the presence of the small gold protrusions and indentations, the mean diameter found from AFM data is smaller than the XRD crystal size.

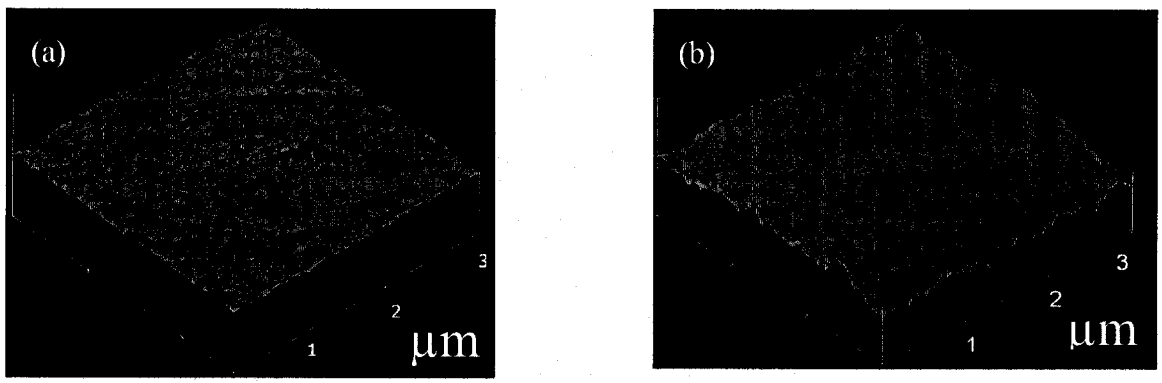

Figure 5.8 *The surface plot of a) 750 nm composite film as compared with b) corresponding Au film.*

5.1.3 Structure of the Composite (type B) on a Silicon Substrate

Figure 5.9 shows the XRD of a composite film prepared by coating the Au film with four layers of SnO_2 (n = 4). Strong substrate peaks can be seen near 20 nm^{-1} (Si 111), 40 nm^{-1} (Si 222) and at 60 nm^{-1} (Si 333). Comparison of the intensities of the gold lines with the powder average for gold (JCPDS 04-0784), obtained from International Center Diffraction Data (ICDD) or formerly known as

(JCPDS) Joint Committee on Powder Diffraction Standards which is the organization that maintains the data base of inorganic and organic spectra, shows that the gold is preferentially (111) oriented such that the densest layer of gold atoms in the gold crystal is about 800 times less than the intensity expected based on the powder average.

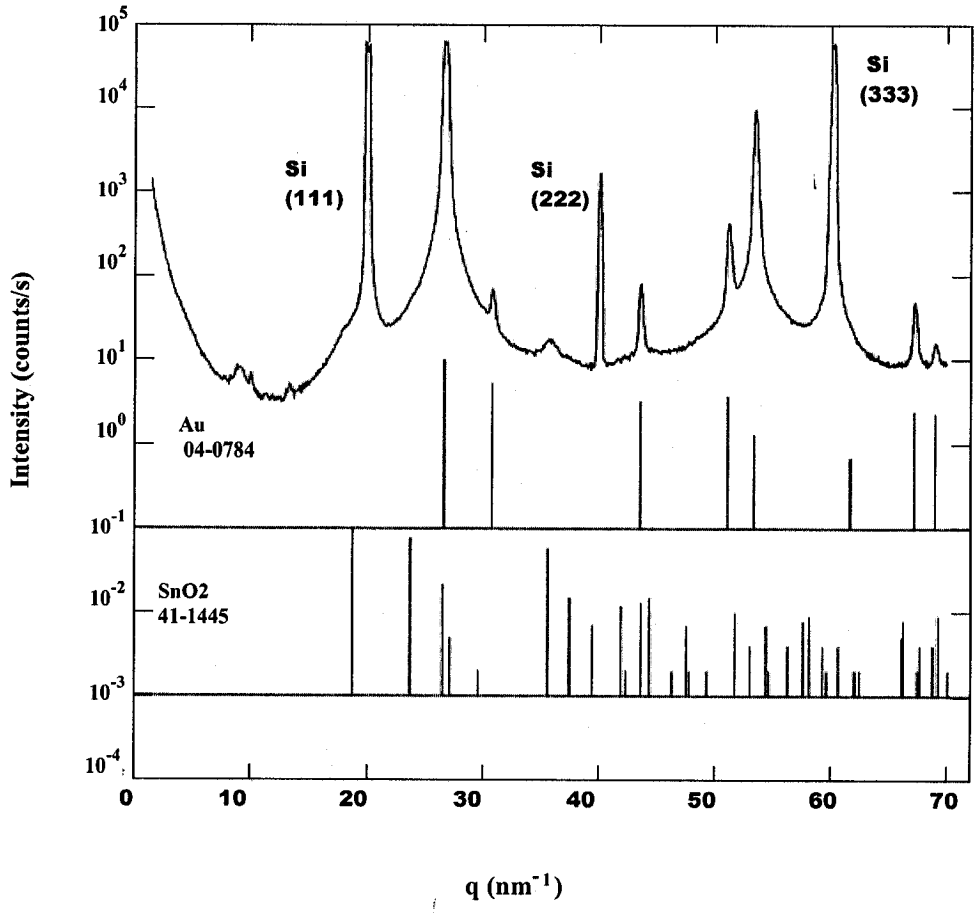

Figure 5.9 *Comparison of intensities of Si, Gold, and Tin Dioxide*

This matter confirmed by the rocking curves around the gold (111) and silicon (111) peaks (Figure 5.10), which shows that the (111) direction gold

grains are aligned to within 3.5 degrees half width at half maximum from the axis perpendicular to the substrate wafer.

Extrapolation of gold peak widths to q=0 resulted in a crystal size of about (46 ± 11) nm. The width of the gold peaks increases with q, and the slope of this increase corresponds to a strain or variation of the lattice constant of 0.11%. Two tin dioxide lines (Cassiterite, JCPDS 41-145) are seen: Cassiterite (110) as a shoulder on the first Si (111) peak, the other as a broad peak near 35.62 nm^{-1} (211). The size of the SnO_2 nanocrystals is found to be (17 ± 6) nm. The size of the crystals from XRD measurements is prone to a quite large error; factors such as crystallite shape, orientation distribution, etc., may have an influence on the accuracy of the results.

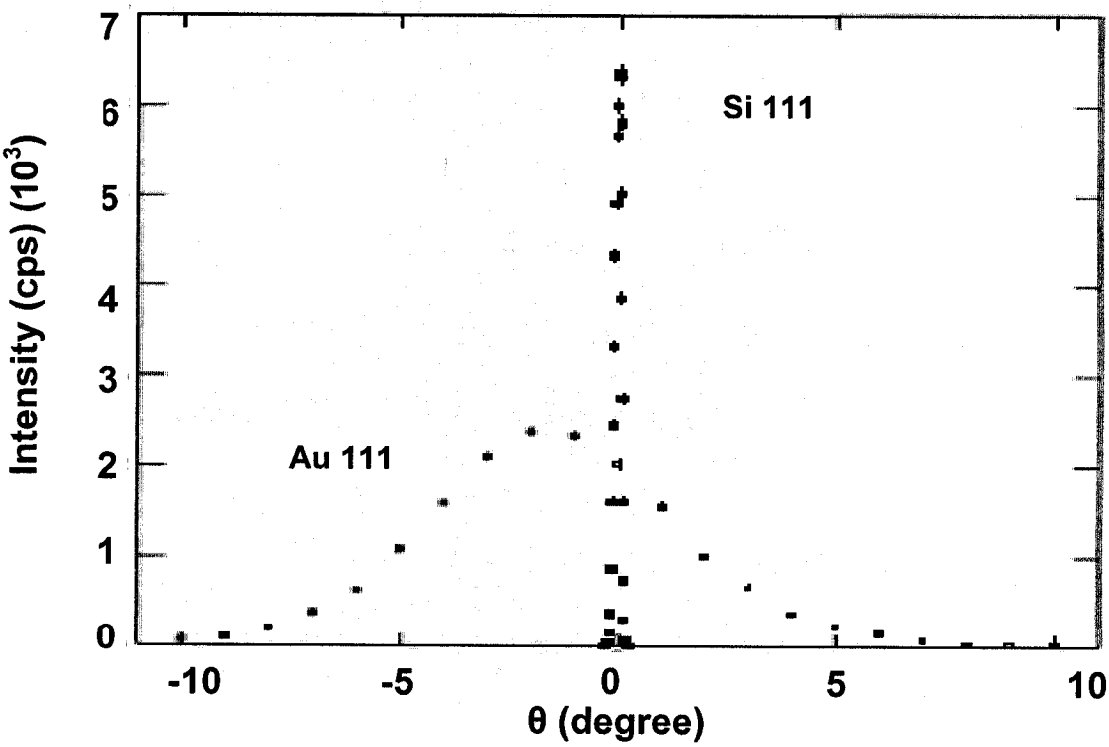

Figure 5.10 *The Rocking curve of the sample of gold and tin dioxide on the silicon substrate*

5.1.4 Micro-Raman Spectroscopy Study of the Au/SnO_2 Composite (type B)

The presence and location of SnO_2 nanocrystals has been evidenced by micro-Raman measurements (Figure 5.11 and 5.12).

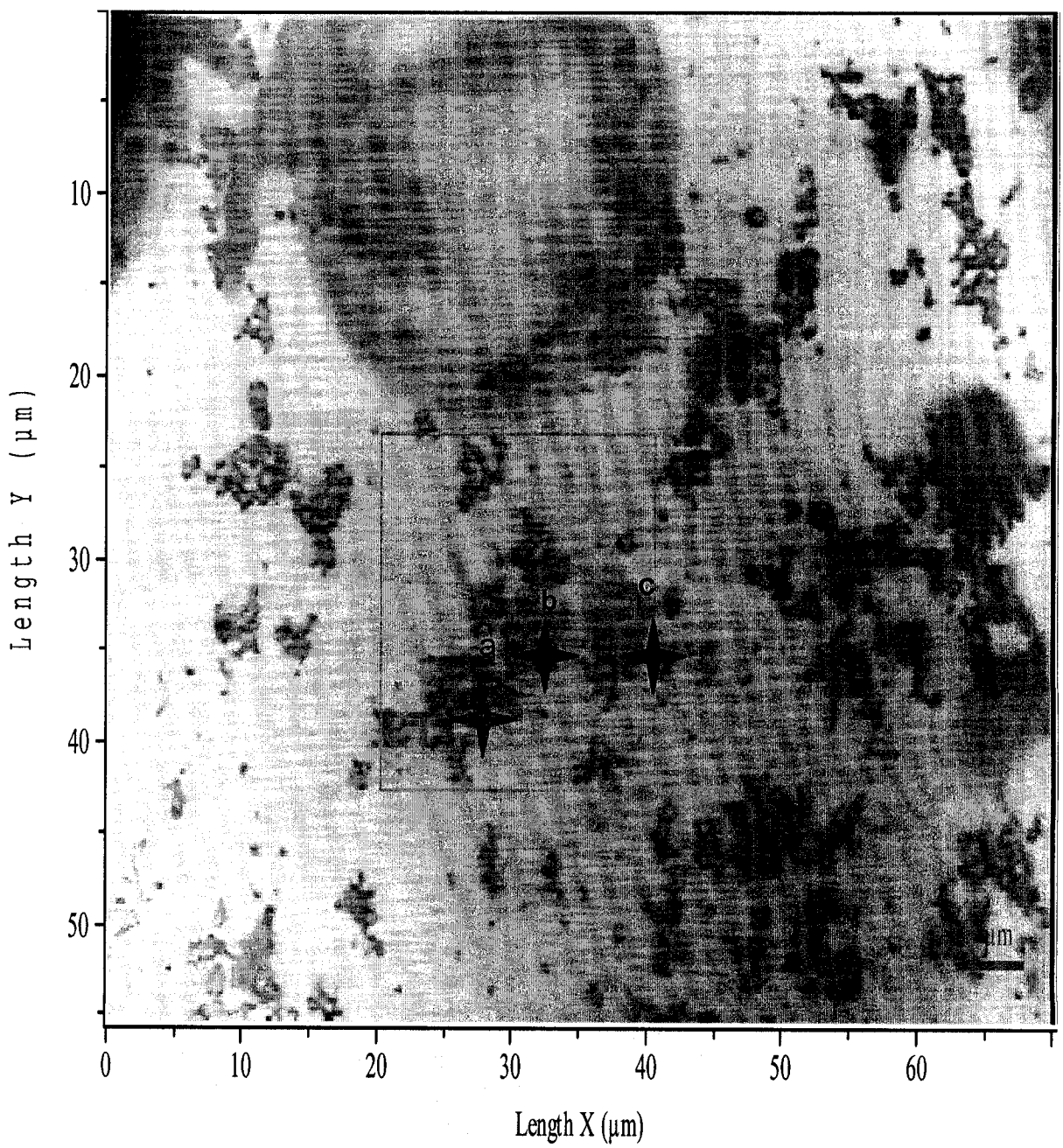

Figure 5.11 *The optical surface of sample (Si/Au/SnO_2)*

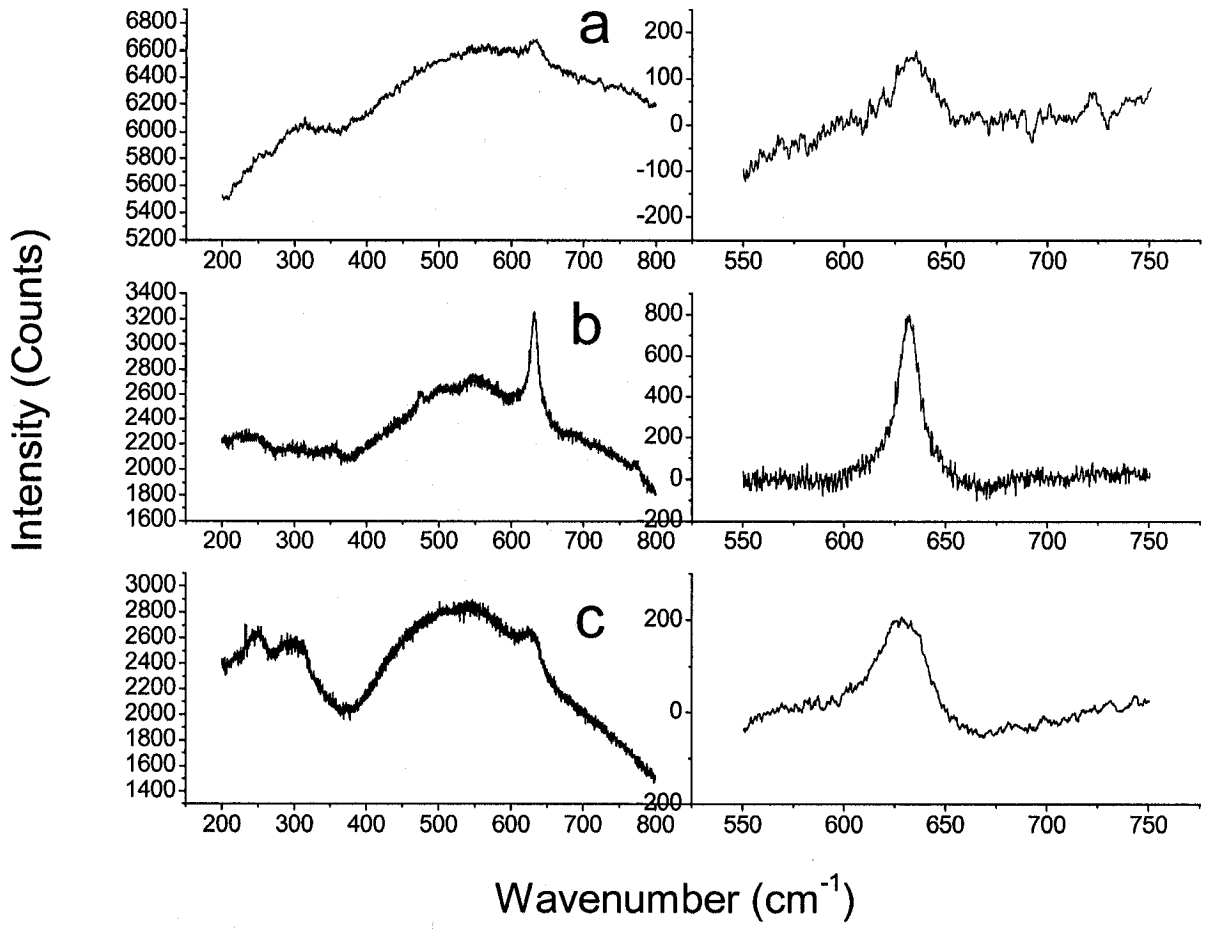

Figure 5.12 *The Raman spectra of three different areas of a sample*

The Raman spectra show the following modes: 253.7, 310.5, 476, 634.6, and 772 cm^{-1}. Among these, the 476, 634.6 and 772 cm^{-1} peaks are attributed to the Raman bands of crystalline SnO_2 [29]. It should be noted that the most intense Raman peak (634.6) of SnO_2 is blue shifted by 4 cm^{-1} when compared with the crystalline SnO_2. An interesting observation is the appearance of lower energy modes at 253.7, and 310.5 cm^{-1} and of the broad band observed between 400 and 800 cm^{-1}. The origin of the lower wavenumber modes has not been well understood. Many authors have discussed the origin of these modes. A plausible

explanation for these modes would be related to the very small size of SnO_2 crystallites.

Rumyantseva et al [30] have observed the low energy modes during the Raman studies on the nanocrystalline SnO_2 powders (particle size of 9 nm) heat-treated at 500 °C. They have found that these modes vanished when SnO_2 was heated at higher temperatures and attributed them to Raman inactive modes in nanocrystalline SnO_2, which are otherwise absent in bulk crystalline SnO_2. Further, the broad band between 400 and 800 cm^{-1}has been attributed to the surface modes of SnO_2 particles. According to Rumyantseva et al [31], the intensity of the broad band decreased linearly with an increase in the particle sizes, and this observation is in good agreement with the gas sensing ability of SnO_2. Thus, both the lower energy modes and the surface vibrational modes observed in the spectra emphasize the formation of nanocrystalline SnO_2. The Raman mapping shows the presence of tin dioxide particulates non-uniformly distributed over the region shown in Figure 5.11. The spectra were recorded from three selected points color-coded in the rectangular box shown inside the optical microscopic white light image. The band observed at 634 cm^{-1} corresponding to the A_{1g} mode is the most intense mode for SnO_2 and has been used to calculate the intensity enhancement. This band is shown in the second column of Figure 5.12 after the base line correction was done. The intensity of the base line-corrected peaks ranged from 150 to 800 counts and it was compared to the 634 cm^{-1} peak intensity of SnO_2 coated directly on the Si substrate, i.e., without the Au film (Figure 5.13).

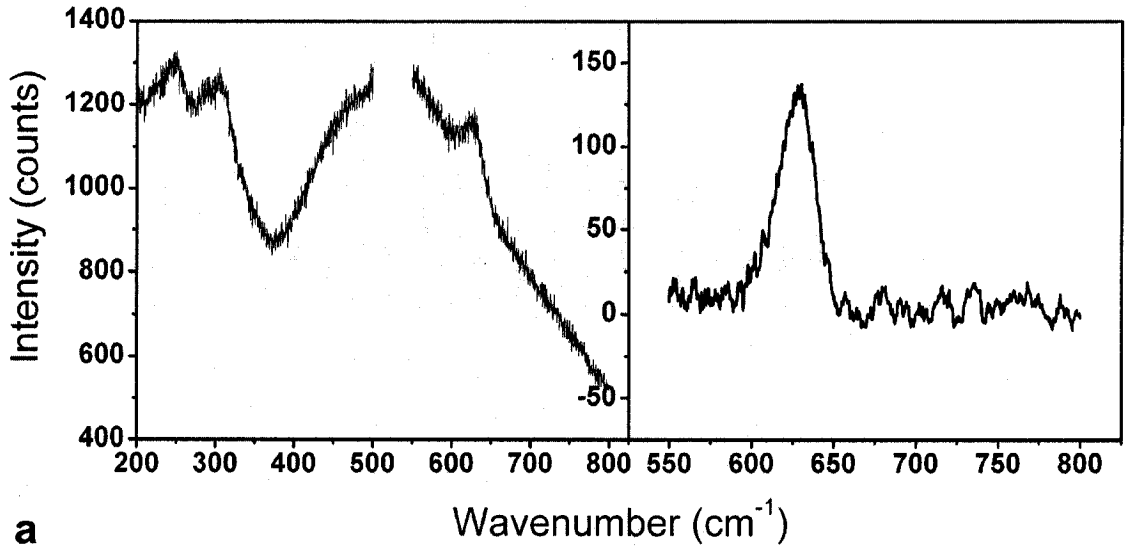

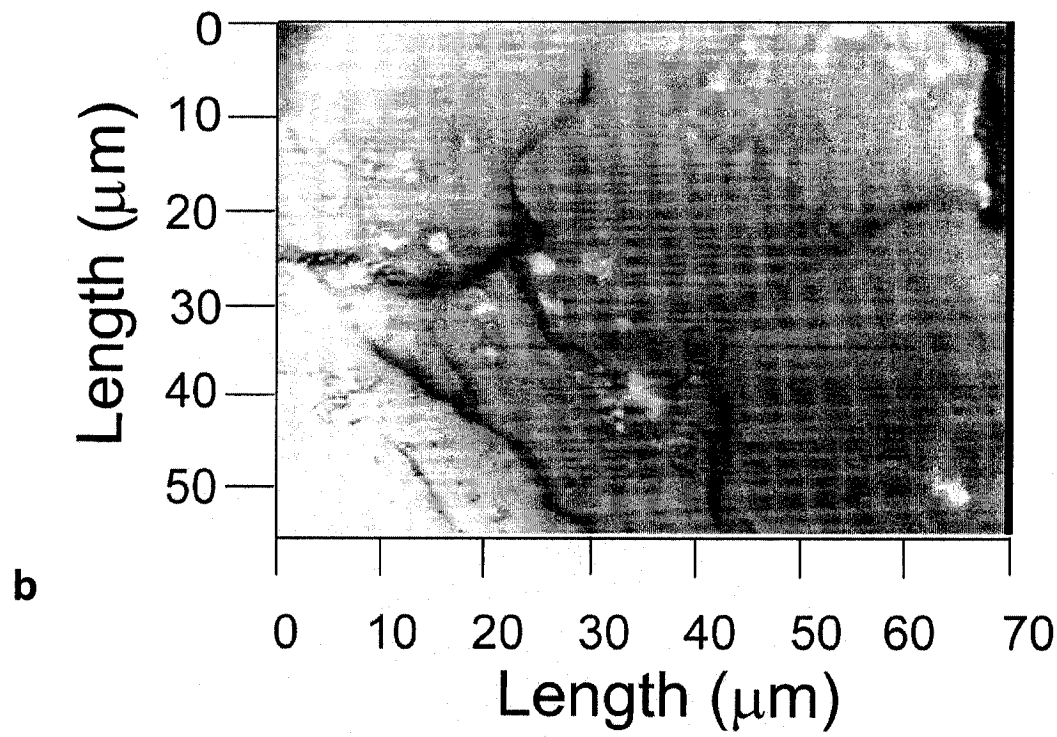

Figure 5.13 *a) Raman spectrum, b) white light optical microscopic image of SnO_2 particles on the Si substrate*

The spectrum of SnO_2 particles on the Si substrate is shown in Figure 5.13 a along with the white light optical microscopic image (Figure 5.13 b).

After the base line correction, this spectrum was used as a standard to calculate the enhancements due to the Au underlayer. The results indicated that only the Raman signal from point b showed an enhancement (by 6 times) while the signals from the other two points (a and c) showed no significant enhancements.

5.1.5 FTIR Spectra of SnO_2 on a Glass Substrate

Figure 5.14 shows the infrared spectrum of tin dioxide coated on a glass substrate and, subsequently, annealed at 200^0C. The spectrum indicates that the sample annealed at this relatively low temperature still contains some residual organic groups that originate from the precursor used in the sol-gel synthesis. The wide absorption around 1100 cm^{-1} composed of several absorptions, may have contributions from the 1390 cm^{-1} and 1370 cm^{-1} bands assigned to the symmetric bending vibrations of the C-H bonds of the tert-butoxy groups [32]. A weak band at 1255 cm^{-1} belonging to the skeletal vibrations of the tert-butyl group is part of the wide absorption as well. In the high-frequency region of the spectrum, there is a broad band between 3350 and 3450 cm^{-1} corresponding to υ_{OH} , the stretching vibrations of OH groups. The strong bands observed at 673 and 624 cm^{-1} were assigned to Sn-O-Sn and Sn-O vibrations [33].

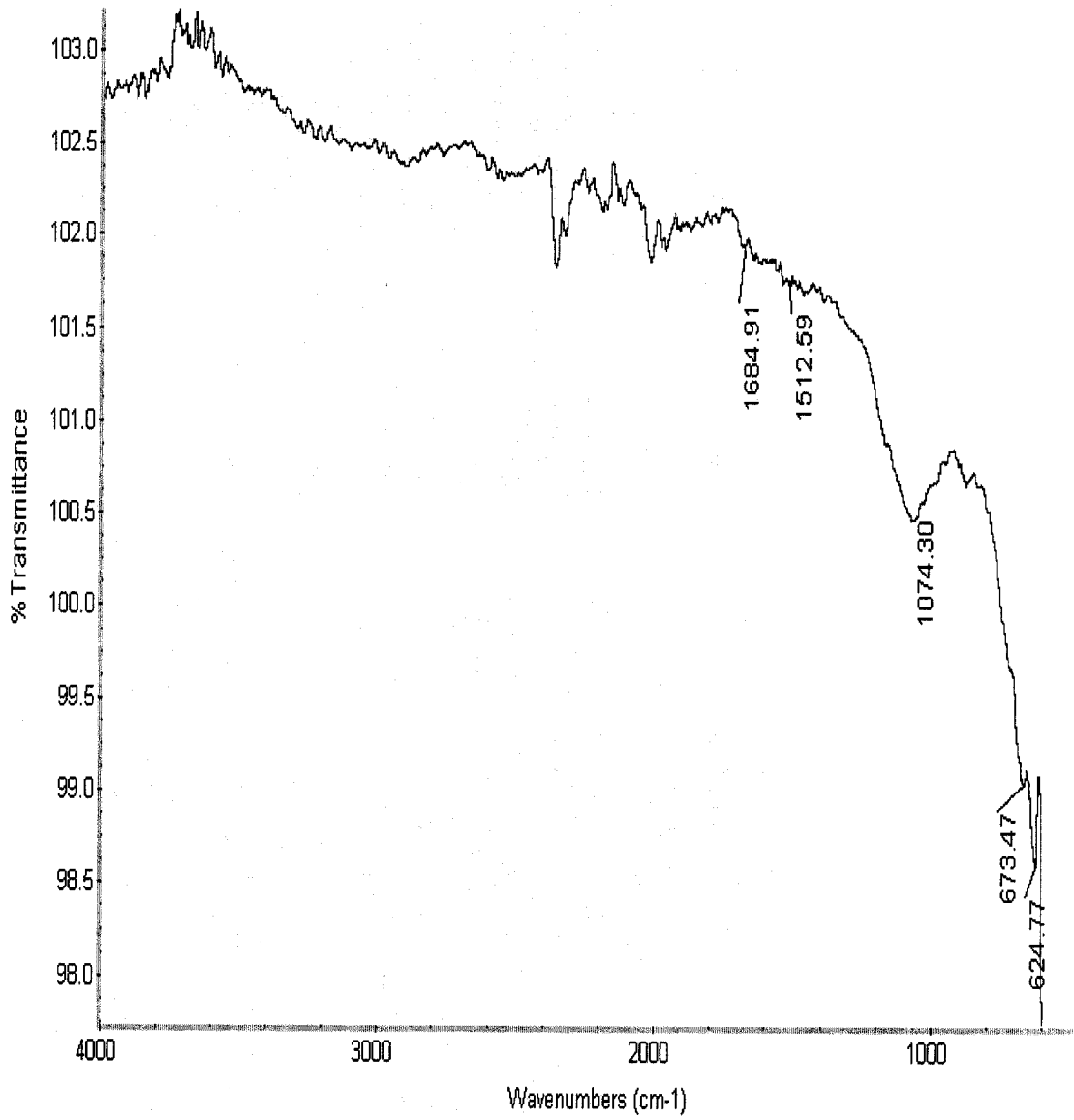

Figure 5.14 *The infrared spectrum of tin dioxide coated on a glass substrate annealed at 200^{0}C*

In Figure 5.15 the infrared spectrum of tin dioxide annealed at 500^0C is given. The spectrum shows the presence of only two strong bands at around 725 cm^{-1} and 860 cm^{-1}.

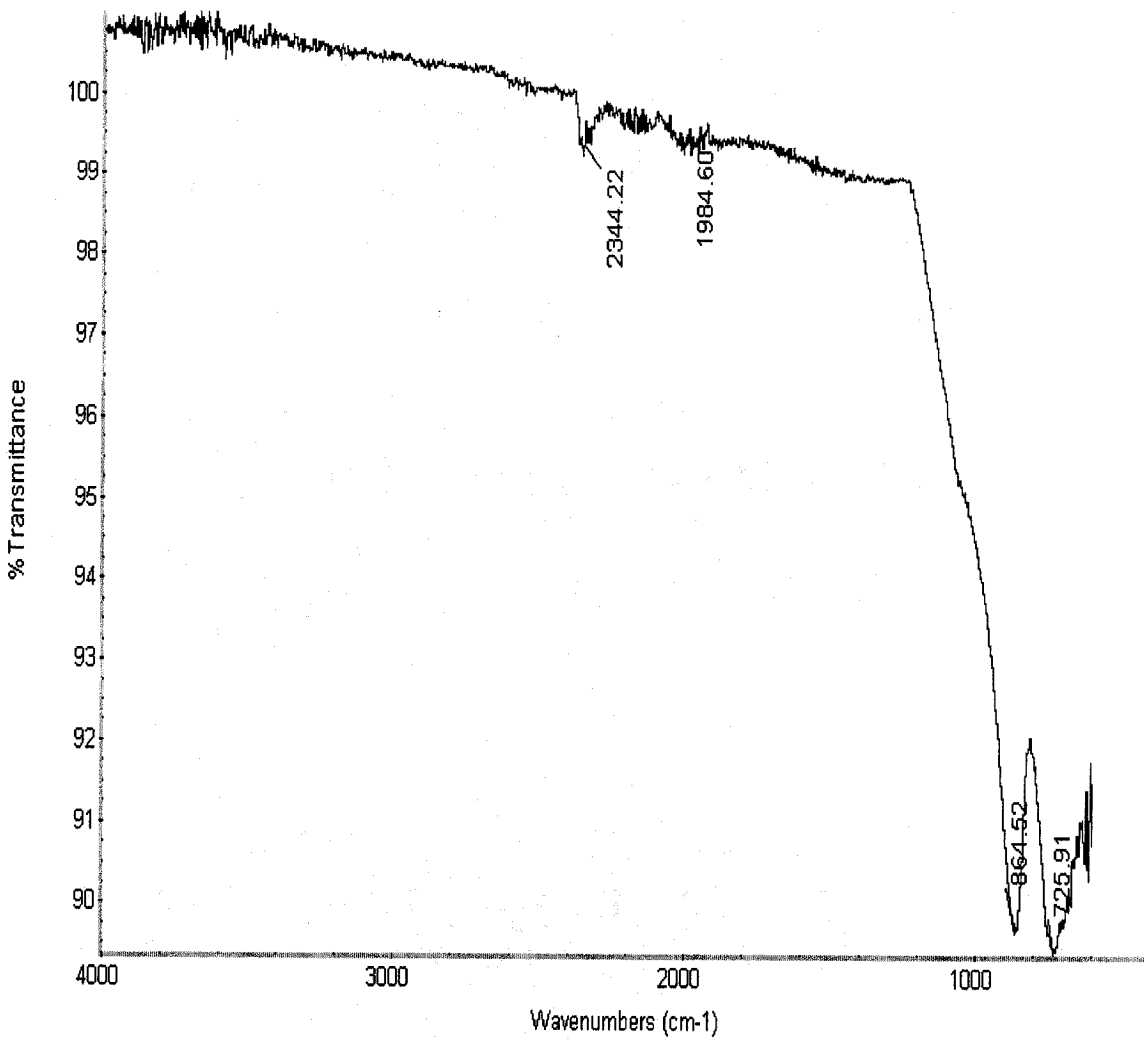

Figure 5.15 *The infrared spectrum of tin dioxide annealed at 500^0C*

These bands can be assigned to Sn-O stretching bands of SnO_2 nanocrystallites aggregated at 500^0 C. As found from XRD line broadening, the crystallite sizes of SnO_2 on gold were in the range of 17-20 nm. Since AFM measurements showed structural units of large spherical particles, it was

concluded that very fine SnO_2 crystallites (as shown by micro-Raman spectroscopy as well) are structural units of larger particles. It has been shown [34] that the spectral features of SnO_2 depend both on the route of synthesis and the temperature of the post heat treatment. The authors have demonstrated that with an increase of the crystallite size and the overall crystallinity, the Sn-O stretching bands appear to be shifted to higher wavenumbers. They have shown that for samples prepared by the sol-gel route and annealed at 400^0C, broad bands centered at 611 and 603 cm^{-1} were observed.

5.1.6 Reflection Spectra of the Au/SnO_2 Composites

Figure 5.16 shows the first derivative of the differential near-normal incidence reflection spectra (ΔR = reflectivity of Au surface – reflectivity of Au surface coated with SnO_2) of the Au/SnO_2 composite prepared by coating the Au film with tin dioxide films of increasing thicknesses (1-4 dips).

In the case of the thick Au film (composite B), it can be seen that, with increasing number of deposited layers of SnO_2, the SPR band appears slightly shifted to longer wavelengths (from 500 to 510 nm). At the same time, the results show a strong increase in the intensity of the gold SPR band when the thickness of SnO_2 is increased through multiple dipping. On the other hand, it can be seen that, with increasing number of layers, the full-width at half-maximum (FWHM) and therefore, the asymmetry of the band decrease significantly. Indeed, in the case of tin dioxide coated on the 750 nm thick film, the FWHM decreased from 158 nm (one dip) to 55 nm (four dips). It is interesting to also note that the degree of agglomeration of gold decreased with increasing number of layers.

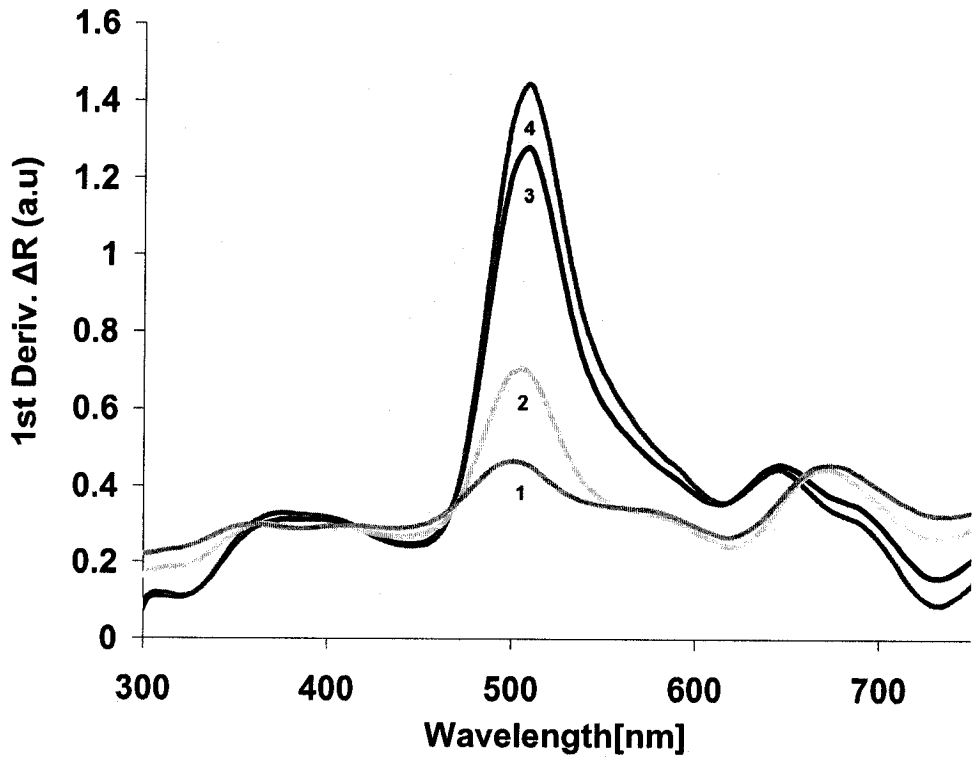

Figure 5.16 *The 1st derivative of ΔR for the Au/SnO_2 composite prepared by coating the Au film with tin dioxide films of increasing thicknesses (1-4 dips)*

This is indicated in the spectrum by a blue shift of the band characteristic to aggregated Au from 672 nm to 645 nm. In addition to the observations regarding the properties of the SPR band of gold, the intrinsic properties of tin dioxide are altered as well when it is coated on Au. The band gap absorption in the SnO_2 – coated gold appears to be redshifted in the composite and extended from 357 nm (one layer) to a broad absorption between 375 nm and 400 nm (4 layers). The results appear quite different for a thin (170 nm) Au film coated with SnO_2 (composite A, not shown here). In this case, the strongest effect on the SPR intensity is seen for the first layer (1 dip) of tin dioxide. The FWHM as well as the intensity values are less affected by the next layers and no effect of gold on the tin dioxide band gap absorption is seen in the spectrum. In other words,

when the gold film is thin, the optical properties of the composite are much less sensitive to the thickness of SnO_2 than in the case of a thicker film.

Three major factors are expected to contribute to the broad spectral response of the plasmon: homogeneous broadening due to electron surface (interface) scattering, inhomogeneous broadening due to nanoparticle size and shape distribution, and chemical interface damping related to the influence of the local chemical environment at the nanoparticle interface [35]. As the total (Au + SnO_2) particle size is much smaller than the wavelength of the incident light at resonance, in the case of the Au/SnO_2 composite, phase retardation effects are irrelevant. In addition to electron surface scattering, a dominant contribution to the linewidth would come from the statistical variations in particle size and shape, experimentally inevitable for both the Au and SnO_2 particles.

According to AFM results, the size distribution scales inversely with the SnO_2 thickness, that is, the broadest distribution corresponds to the composite with the thinnest layer of SnO_2. Increasing the thickness of the layer through further dip-coating, the size distributions become narrower, in agreement with the experimental band width. Although the AFM images clearly show the presence of particles with different shapes, the shape distribution cannot be well-quantified. However, it is reasonable to assume that the statistical variations in particle shape will contribute to the experimental linewidth as well.

The simulated reflection curves are given in Fig 5.17 and the effective medium parameters used for the simulation are given in Table 5.1.The model used in the simulation as well as the precise meaning of the parameters are given in Chapter 2. As it can be seen, η, the distance separating the induced

dipole moment and its mirror image divided by the rotational axis of the ellipsoid, was kept constant at 0.8. As a first approximation, the particles can be considered as spheres with a real depolarization factor of 1/3. Optical constants for Au were given by Ref [36] while these for SnO_2 were provided by Ref [37].

The simulated curves show that the change of the thickness and filling factor Q corresponding to successive dips does not provoke a significant change in the position of the gold plasmon band. Indeed, an increase of Q from 0.28 (1 dip) to 0.37 (4 dips) red shifts the SPR band by less than 10 nm, in agreement with the experimental results. The band characteristic to the aggregated gold (between 600 and 700 nm) however, is not affected by the change of the parameters. The change in the band gap absorption of tin dioxide as revealed by the experimental curves is shown by the theoretical curves as well. The band gap absorption that is around 320 nm in curves 1 and 2, appears centered around 340 nm in curve 4 corresponding to a filling factor of 0.37.

In general, we can conclude that the model used for the calculation represents a reliable description of the real system and, consequently, the simulated curves compare well with the experimental results.

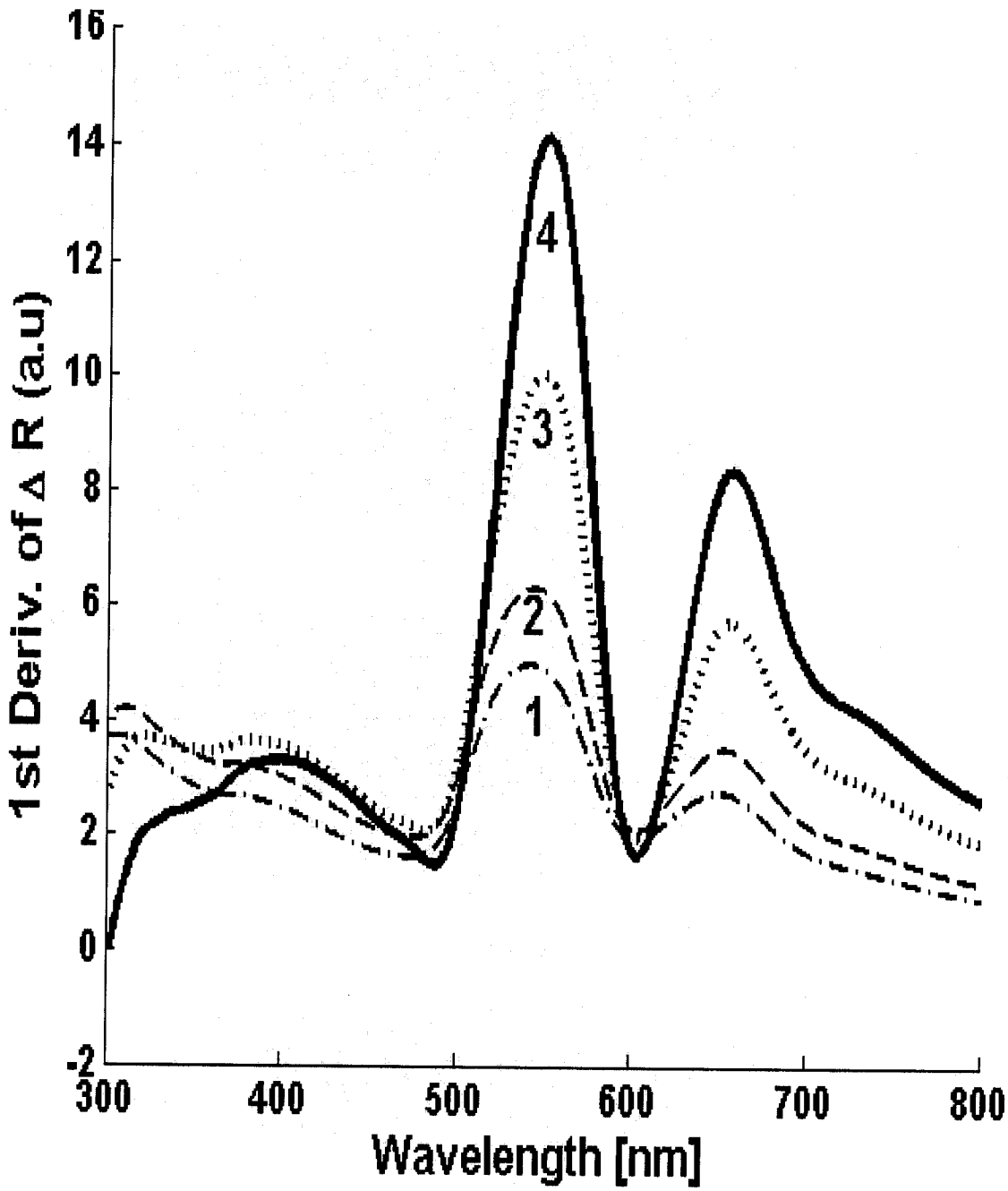

Figure 5.17 *The 1st derivative of ΔR for the Au/SnO_2 composite prepared by coating the Au film with tin dioxide films of increasing thicknesses (1-4 dips) simulated by MATLAB*

Number of Coating	η	Q	γ	d [nm]
1	0.80	0.28	1.80	35
2	0.80	0.30	1.85	38
3	0.80	0.33	1.90	43
4	0.80	0.37	2.00	45

Table 5.1 *Effective medium theory parameters used for the simulation*

5.2 Titanium Dioxide Particles on Silver Surfaces

5.2.1 Structure and Morphology of the Ag/TiO_2 Composite

Figure 5.18 shows the AFM image of the Ag/TiO_2 composite (Figure 5.18 a, b) together with the size distribution (Figure 5.18 c). The AFM data on a pure TiO_2 film on a glass substrate is shown for comparison purposes (Figure 5.19). For the composite, the AFM micrographs (Figure 5.18 a, b) show distinct spherical TiO_2 particles intermingled with the larger silver grains. The silver grains have probably smaller indentations on the top resulting in an extremely narrow size distribution (Figure 5.18 c). The average nanocrystalline size as found from the distribution over a broad range is around 4 nm which correlates well with the crystallite size calculated by the Sherer equation from the XRD line broadening. The morphology of the silver film 100-300 nm thick depends on the nature of the substrate.

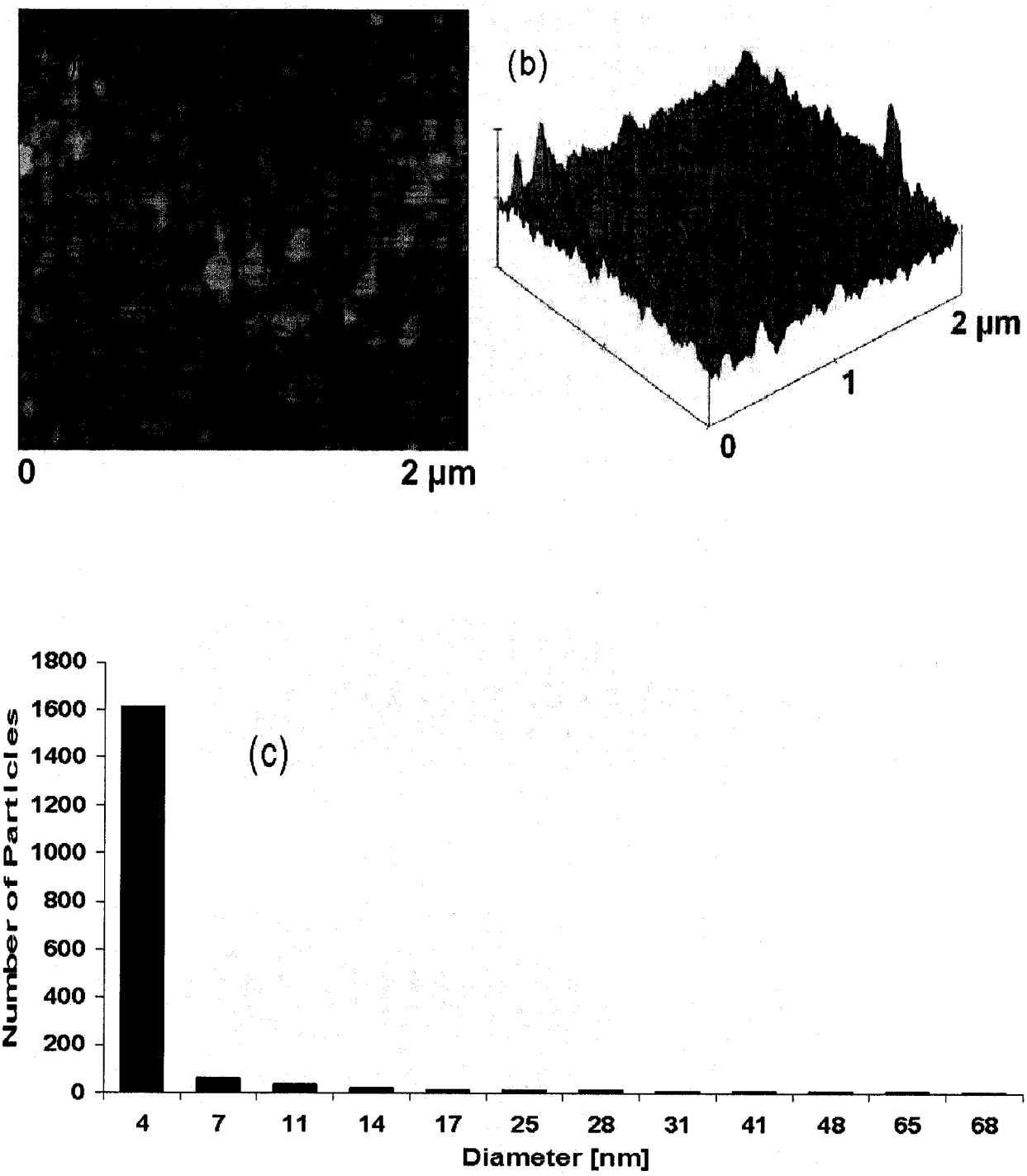

Figure 5.18 *AFM images of the: (a and b) Ag/TiO_2 composite, (c) the particle size distribution*

The AFM images of TiO_2 thin films on glass substrate reveal a distinct change in the surface morphology as shown in Figure 5.19 a and Figure 5.19 b.

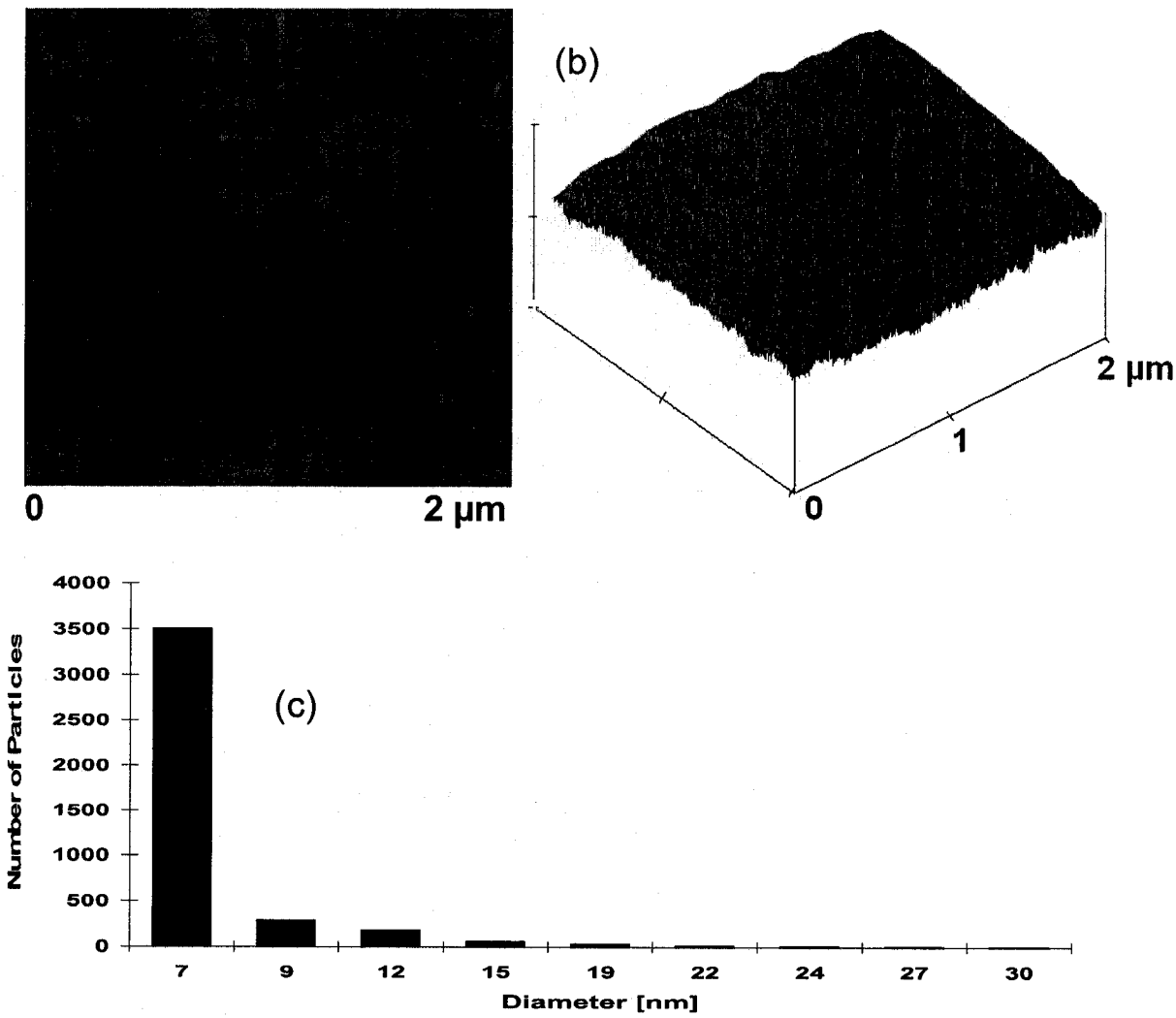

Figure 5.19 *AFM images of the: (a and b) TiO_2 on a glass substrate (c) The particle size distribution*

The surface of the film appears to be made up from particles of different sizes and shapes and the size distribution (Figure 5.19 c) became broader than in the case of the TiO_2 dip-coated on the Ag film. The mean particle size was

found around 7 nm and larger particles were found in the image as well. Both the films (on glass and silver) are smooth: the mean roughness (R_a) of the titania film on silver is found to be around 4 nm, larger than that on the glass (1.7 nm). The particle height (out-of-plane height) as found with the AFM software is around 45 nm for the titania on the silver and considerably smaller for the TiO_2 film on glass (around 10 nm).

5.2.2 XRD Study of TiO_2 Film on Ag

Figure 5.20 shows the X-ray scattering from a glass slide with a 120 nm sputtered silver coating, and two Ag/TiO_2 composites with sputtered silver thicknesses of 153 nm and 204 nm. The data are shown as a function of the modulus of the scattering vector, and the scattering from an empty glass substrate has been subtracted from the measured intensities. JCPDS reference powder patterns are shown for fcc silver and anatase (JCPDS 04-0783 and 21-1272, respectively).

The films were deposited on glass substrates, and the scattering from an empty glass substrate was subtracted from the signal. The fcc silver peaks are clearly seen, and the peak broadening correspond to crystallite sizes of 20±5 nm as calculated by the Scherrer equation. A broad peak near q = 18 nm^{-1} indicates the presence of small anatase crystals in the TiO_2 coated films, and for the 153 nm thick film the anatase peaks near 33 and 37 nm^{-1} can also be identified. The anatase crystal sizes calculated from peak broadening are 5.1±0.3 nm for the 153 nm thick film, and 3.7±0.5 nm for the 204 nm thick film.

The relative intensities of the (111) and (200) fcc-Ag peaks for the sputtered film without the TiO_2 coating are close to the powder average (JCPDS

pattern 04-0783). In the case of the TiO_2 coated films the Ag crystallites are oriented preferentially in the (100) direction, based on an enhancement of the (200) peak intensities. This enhancement is particularly strong for the 153 nm thick sample, where the (200)/(111) peak intensity ratio is about ten times larger than the ratio for the powder average.

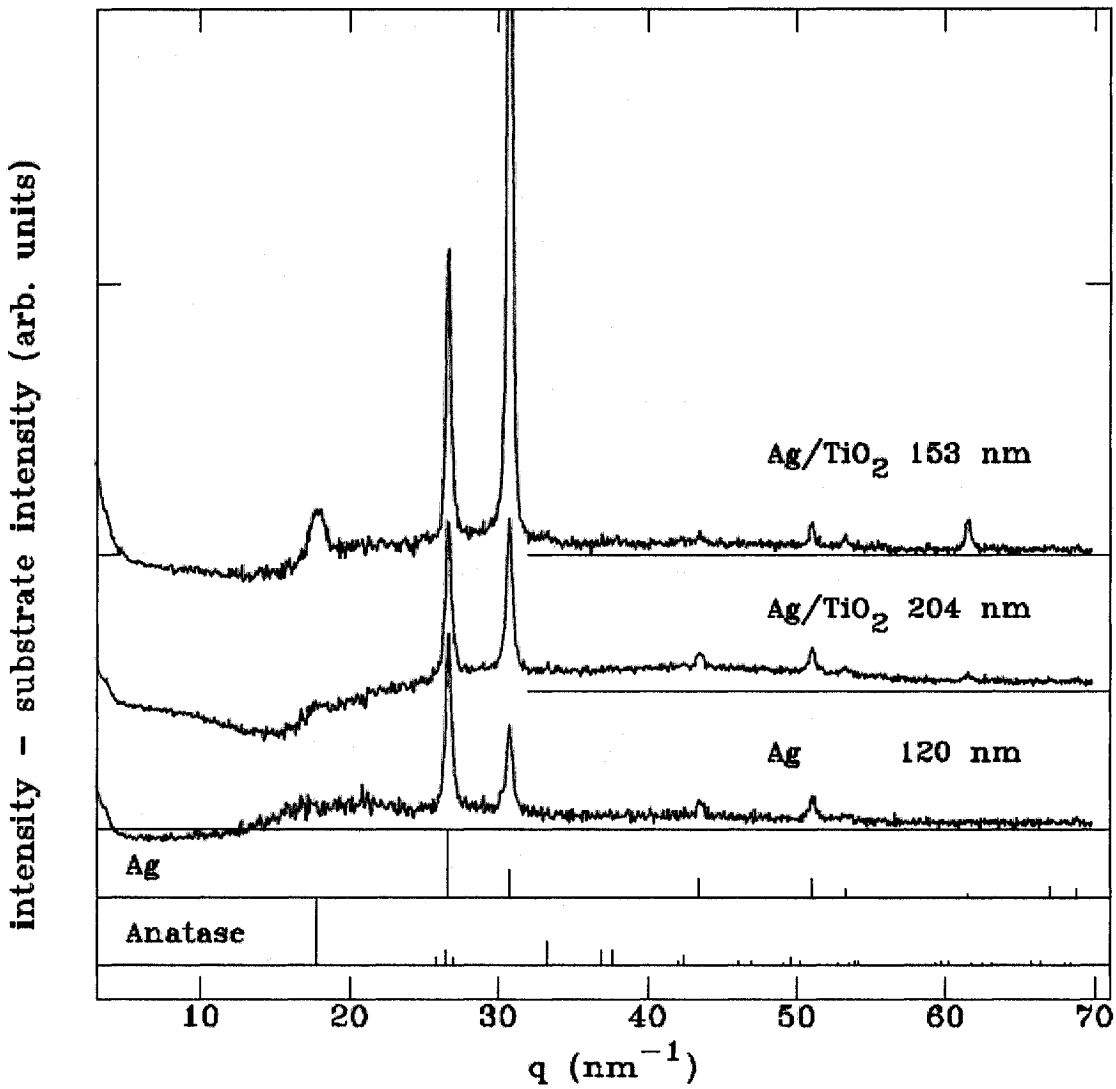

Figure 5.20 *X-ray scattering from a glass slide with a 120 nm sputtered silver coating, and two Ag/TiO_2 composites with respective sputtered silver thicknesses of 153 nm and 204 nm*

5.2.3 Micro-Raman Study of TiO_2 Film on Ag. Estimation of the TiO_2 Crystallite Size with a Phonon Confinement Model

The white light optical image of the TiO_2 film coated over the Ag substrate (thickness of Ag = 204 nm), is shown in Figure 5.21.

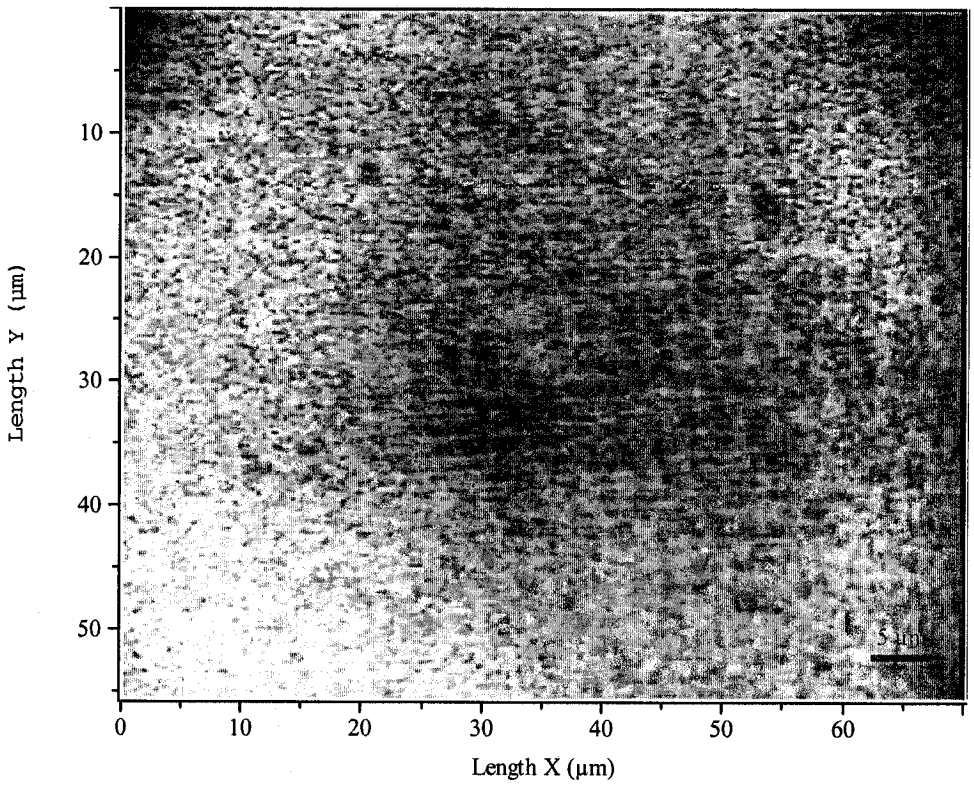

Figure 5.21 *White light optical microscopic image of the TiO_2 film coated over Ag substrates (thickness of 204 nm)*

The Raman intensity of the TiO_2 film on a Ag coated surface is shown in Figure 5.22 a while the one for the TiO_2 film on a glass surface is shown in Figure 5.22 b. The films were fairly uniform on the Ag coated side but with colored features. This colored feature can be attributed to the thickness of the film. The Raman intensity of TiO_2 film on Ag surface is 19.4 times higher than the Raman intensity of TiO_2 film on the glass surface. This is estimated from the main

Raman line of anatase TiO_2 which exists at 148.5 cm^{-1}. The peak position of this mode is blue shifted when compared with the commercial TiO_2 anatase powder. This shift is attributed to the nanometer size of the crystallites [38].

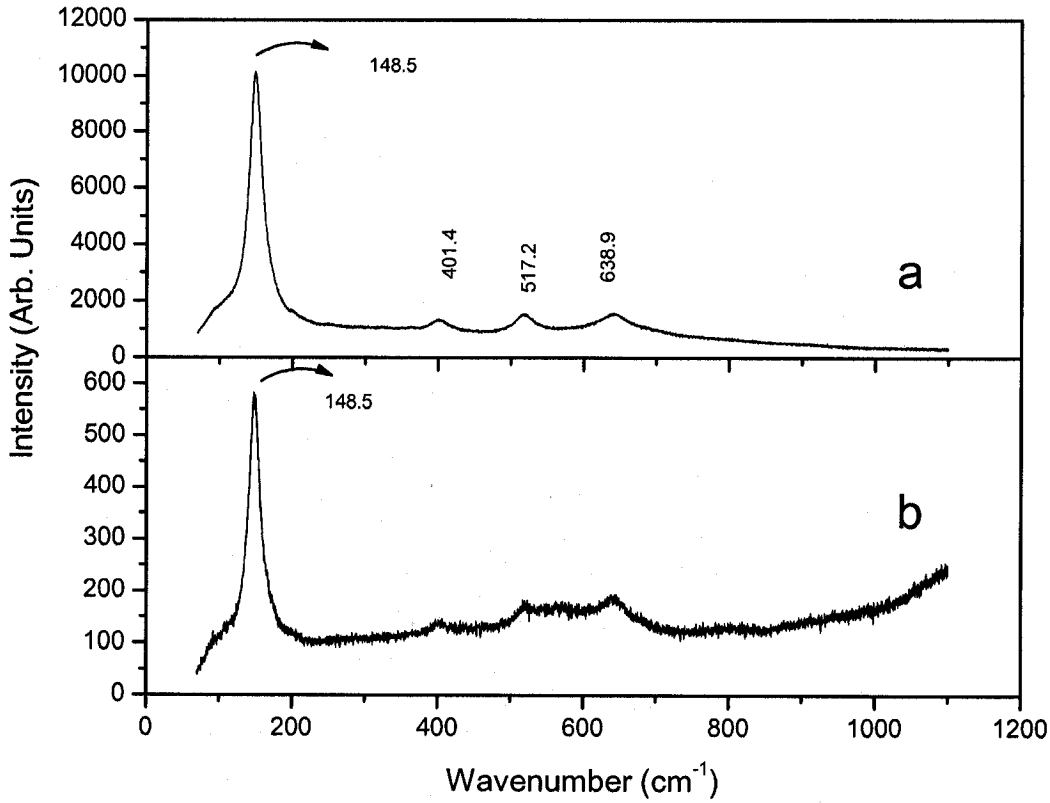

Figure 5.22 *Raman spectra of the TiO_2 films coated over: (a) the Ag substrate (thickness of Ag = 204 nm), and (b) the glass surface*

The white light optical image of the TiO_2 film coated over the Ag (thickness 153 nm), is shown in Figure 5.23. This figure shows a typical state of the TiO_2 film, state that can be reproduced over a large number of samples.

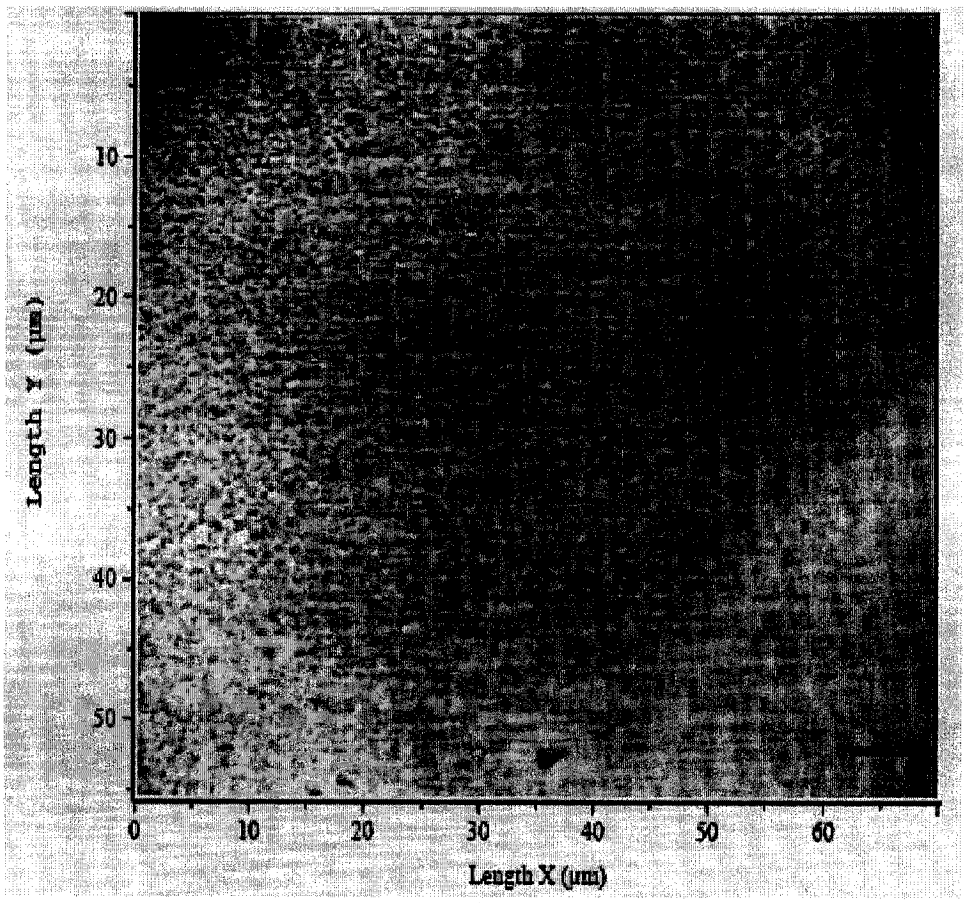

Figure 5.23 *White light optical microscopic image of the TiO_2 film coated over Ag substrates (Ag thickness of 153 nm)*

The Raman intensity from the regions where a TiO_2 film exists on a Ag coated surface (shown in Figure 5.24 a) is much higher than the Raman intensity from the TiO_2 film on the glass surface (shown in Figure 5.24 b). This is estimated from the intensity main Raman line of anatase TiO_2 which exists at 148.5 cm^{-1}.

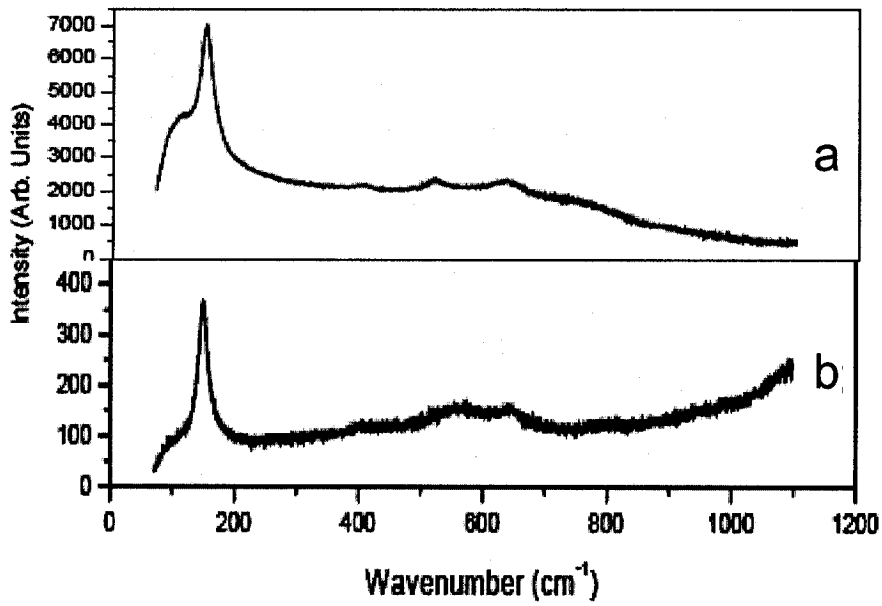

Figure 5.24 *Raman spectra of the TiO_2 films coated over: (a) the Ag substrate (thickness of Ag = 153 nm), (b) the glass surface*

For all the samples the TiO_2 samples (Table 5.2) coated on the Ag layers, the higher intensity anatase Raman band is very broadened (up to ~23 cm^{-1}) and high-frequency shifted (up to ~150 cm^{-1}), displaying the main aspect of nanocrystalline TiO_2 [38], when compared to the Raman spectrum of commercial anatase TiO_2 powder, which has the peak position (PP) at 142.5 cm^{-1} and a full width at half maximum (FWHM) of 7.5 cm^{-1}.

Using a phonon confinement model [39], it is possible to obtain an estimate of the crystallite size from the FWHM and the position of the anatase main Raman peak. The evolution of crystallite size is shown in Table 5.2. In the TiO_2 samples prepared on Ag surfaces, the anatase main Raman peak is centered, respectively, at 149.1, 148.5, 149.7, and 149.9 cm^{-1}, with a FWHM of 23.5 cm^{-1}, 21.3, 21.2, and 21.7 cm^{-1}; each of these gives a crystal size of ~5 nm.

We can attribute such large shifts and broadening of the main Raman band of the anatase phase mainly to the particle quantum size effect [39].

Sample	Raman				XRD	AFM
Ag layer Thickness [nm]	Peak Position [cm^{-1}]	Size [nm]	FWHM [cm^{-1}]	Size [nm]	Size [nm]	Size [nm]
204	149,1	7,2	23,5	5,5	3,7±0.5	5 ±0.5
204	148,5	7,7	21,3	6,1	3,7±0.5	5±0.5
153	149,7	6,8	21,2	6,2	5,1±0.3	4±0.5
153	149,9	6,7	21,7	6	5,1±0.3	4±0.5

Table 5.2 *Crystallite sizes of different TiO_2 on the Ag samples*

The XRD data are in good agreement with the Raman results discussed above. The crystallite size is between 5 and to 8 nm for TiO_2 samples prepared on Ag layers. These results establish that the crystallite sizes are in the nanometer scale.

5.2.4 Optical Properties of the TiO_2 Nanoparticles on a Ag Film

Figure 5.25 shows the near-normal reflection spectra of samples prepared by a single dip-coating of the Ag on glass substrate, using TiO_2 solutions with two different concentrations: 0.5 M and 0.05 M. The dip observed in the reflection spectra at about 314 nm is typical of silver bulk properties and corresponds to the plasma absorption wavelength. As can be observed, there is an additional drop

in the reflection at longer wavelengths and the intensity of the shoulder around 402 nm increases with the amount of titanium dioxide deposited. In the 450-750 nm region the spectrum shows a high reflection with no particular structure.

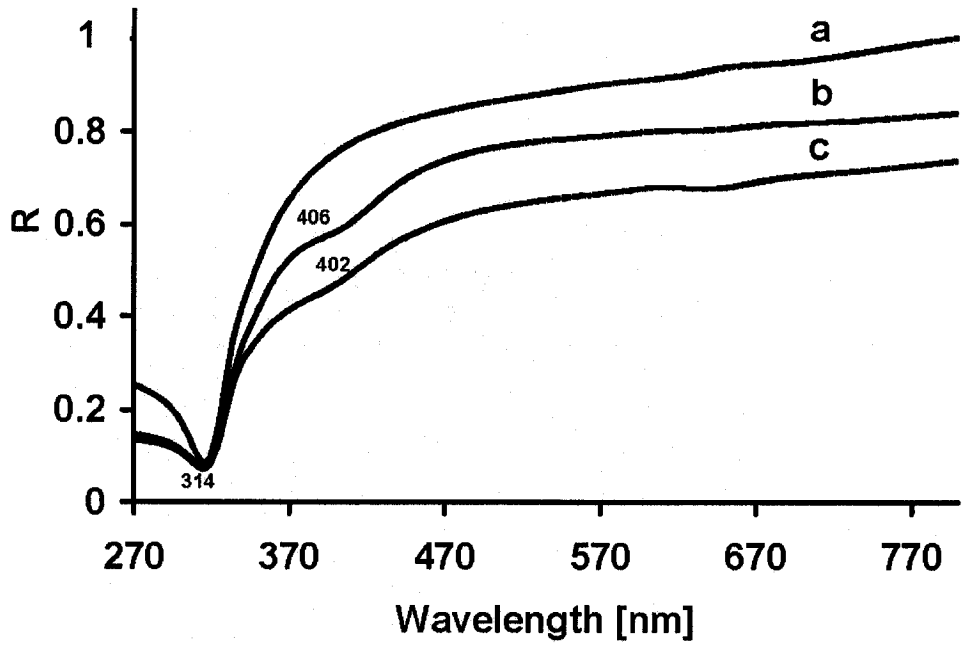

Figure 5.25 *Near-normal reflection spectra of Ag/TiO_2 composites (b, c) and Ag (a).*

An experimental evidence of the resonant absorption is provided by a drop in the near normal reflectance. The parameters used for the simulation are given in Table 5.3 and the simulated curves are given in Figure 5.26. The model used in the simulation as well as the precise meaning of the parameters are given in Chapter 2. As it can be seen, η, the distance separating the induced dipole moment and its mirror image divided by the rotational axis of the ellipsoid, was kept constant at 0.8. In the Table 5.3, γ is the axial ratio or the ratio between the

axis parallel and perpendicular to the film surface plane while Q is filling factor of the dielectric particles and d the thickness of dielectric film (TiO_2).

As a first approximation, the particles can be considered as spheres with a real depolarization factor of 1/3. Optical constants for Ag were given by Ref [36] while those for TiO_2 were provided by Ref [40].

Sample	η	Q	γ	d, nm
b	0.8	0.085	1.7	15
c	0.8	0.090	1.8	20
d	0.8	0.100	1.9	25

Table 5.3 *Effective medium theory parameters used for the simulation*

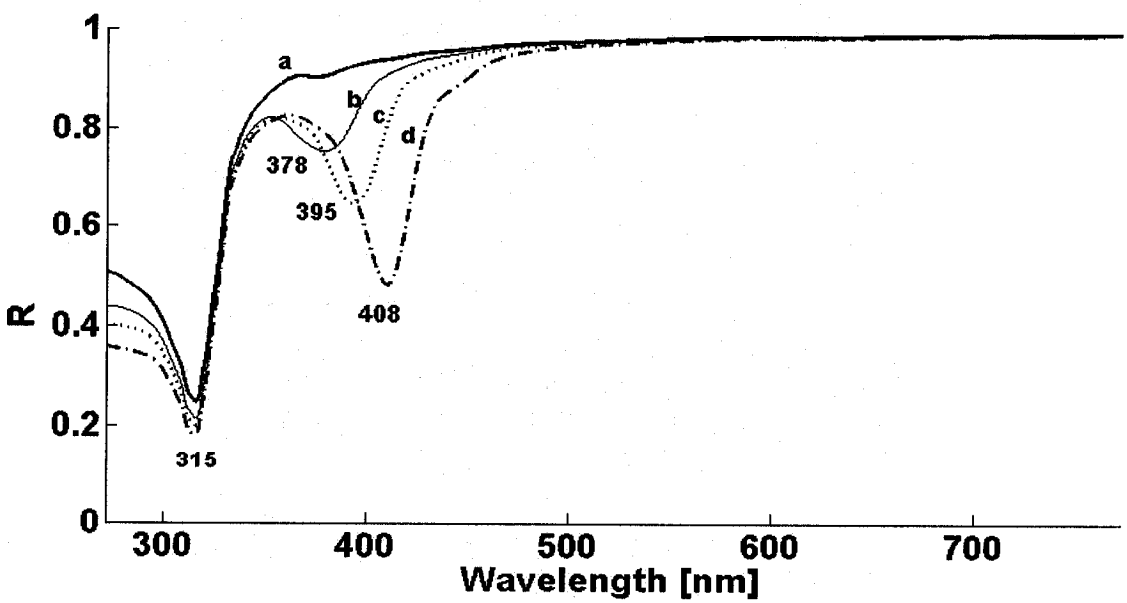

Figure 5.26 *Simulated reflection curves of Ag/ TiO_2 composite (b, c, and d) and Ag (a)*

In the theoretical curves, one can notice that, already with a 15 nm-thick TiO_2 overlayer, there is a drop in the reflection and the peaks are better defined than in the experimental curves (Figure 5.25). By increasing the thickness and the filling factor as well as the axial ratio of the particles, a shift to longer wavelengths of the TiO_2 peak is seen. Overall, there is a qualitative agreement with experimental measurements. We made no attempt to improve further the comparison by introducing, for example, a distribution of particle shape that in principle will broaden the absorption.

The above results have been partly reported in Ref [41].

Chapter 6: Conclusions and Future Directions

Nanolayered systems composed of a gold film coated by a thin granular tin dioxide layer, Au-SnO_2, and a silver film coated by a thin layer of titanium dioxide, Ag-TiO_2 have been fabricated by a combined sputtering/sol-gel method. The principal properties of the nanosystems as shown by the different methods of characterization are:

Au-SnO_2

- Both components are crystalline: Size of the crystallites: Au: 46 ± 11 nm, preferentially (111) oriented on the Si substrate.
- Aggregation phenomena upon heat-treatment on a glass substrate have been evidenced and their effects on the optical properties have been investigated.
- SnO_2: Size of the Crystallites: 17 ± 6 nm (XRD) (Cassiterite), < 10 nm (micro-Raman).
- Size effects due to the nanocrystallinity have been evidenced in the Raman spectrum.
- Enhancement effects of the Raman bands of SnO_2 on the Au substrate have been found.
- Au-SnO_2 : the mean roughness of the film: 7 nm, narrow size distribution (AFM)
- A strong enhancement of the Au SPR band has been found in the near-normal reflection spectra. It has been shown that the position, width and intensity of the Au SPR band strongly depend on the thickness of the tin dioxide layer.

- The intrinsic properties (band gap absorption) of tin oxide have been found altered in the presence of gold.

Ag-TiO_2

- Crystallite size: Ag: 20 ± 5 nm, preferentially oriented (100) on glass.
- TiO_2 : 4 – 5 nm (from XRD, Raman and AFM results)
- Both size and enhancement effects have been found by micro-Raman spectroscopy.
- The near-normal reflection spectra of samples, prepared by a single dip-coating of the silver substrate into the titania precursor solution, show the presence of a well-defined minimum at 314 nm, typical of Ag bulk property and an additional resonant structure at longer wavelengths attributed to surface plasma resonance caused by the presence of the TiO_2 overcoat.
- A very narrow size distribution and no aggregation effect have been found because of the low-temperature sol-gel method employed in the fabrication.
- The optical behavior of the metal surfaces coated by a granular overlayer has been investigated by using the effective medium theory. Simulated reflection curves have been calculated with different parameters and the results showed a very good agreement with the experimental curves for both nanosystems.

The excitation of surface plasmons through the mirror image effects between the dielectric particles and the metallic substrates has been demonstrated for the two nanosystems. The reflection curves corresponding to the two systems showed only a small (10-20 nm) shift of the Au and Ag SPR

bands, respectively. This relatively small shift is accounted for by the physical separation of the two layers in the system. However, because of interface effects, the intensity and the width of the SPR bands have been found very sensitive to the presence and thickness of the dielectric layer. This sensitivity could be exploited in the future in a number of sensor applications. SPR sensors (called also plasmonic sensors) are sensitive to the refractive index of the dielectric medium. The sensitivity and, possibly, the resolution of a plasmonic sensor based on Au may be enhanced with a thin granular overlayer of a dielectric such as tin dioxide or titanium dioxide. It would be especially interesting to use for this purpose plasmonic sensors with intensity modulation that work at a constant wavelength and incident angle. In this context also it would be interesting to conduct the optical measurements with polarized light. As the Ag-TiO_2 system is porous, its utilization as a humidity plasmonic sensor can also be envisaged.

In addition, the nanolayered systems studied in this work may provide a model for the analysis of the optical response of metamaterials. These materials, which are multilayered plasmonic nanostructures containing alternating layers of metal and dielectrics, have been recently proposed as negative index systems, super- and hyperlenses, photonic funnels, and other nanophotonic structures [42], [43].

References

[1] A.V. Krasavin, K.F. MacDonald, A. Schwanecke, and N.I. Zheludev, Appl. Phys. Lett. **89**, 031118 (2006).

[2] R.W. Cohen, G.D. Cody, M.D. Coutts, and B. Abeles, Phys. Rev. B **8**, 3689 (1973).

[3] G. Xu, M. Tazawa, P. Jin, and S. Nakao, Appl. Phys. A: Materials Science&Processing **80**, 1535 (2004).

[4] V.-V. Truong and T. Yamaguchi, Bull. Res. Inst. Electron. (Japan) **25**,1 (1990).

[5] P.V. Ashrit, G. Bader, F.E. Girouard, T. Richard, and V.-V. Truong, J. Appl. Phys. **70**, 3797 (1991).

[6] V.-V. Truong, P.V. Ashrit, G. Bader, P. Courteau, F.E. Girouard, and T. Yamaguchi, Can. J. Phys. **69** (2), 107 (1991).

[7] Y. Xia and N. J. Halas, Mater. Res. Bull. **30**, 343 (2005).

[8] P. N. Prasad, Nanophotonics, (John Wiley, New York, 2004).

[9] V. G. Bordo, in Optics and Spectroscopy at Surface and interfaces, edited by H.-G. Rubahn (Wiley-VCH, Germany, 2005).

[10] A. Otto, Z. Physik. **216**, 398 (1968).

[11] E. Kretschmann, Z. Physik. **241**, 313 (1971).

[12] C. Palmer, in Diffraction Grating Handbook, edited by E. Loewen (Richardson Grating Laboratory, Rochester, 1996).

[13] P. A. Fedders, Physics Review. **165** (2), 580-587 (1968).

[14] G. Binnig, C. F. Quate, and C. Gerber, Phys. Rev. Lett. **56**, 930 (1986).

[15] www.nuance.northwestern.edu/nifit/manuals/htm (June 01, 2007- 5 pm).

[16] http://stm2.nrl.navy.mil/how-afm/how-afm.html (June 02, 2007- 3 pm).

[17] http://course.lib.uci.edu/~mcbrown/xpowder.html (June 10, 2007- 10 am).

[18] B. C. Smith, Fundamentals of Fourier Transform Infrared Spectroscopy, (CRC press, Boca Raton, 1996).

[19] http://www.nuance.northwestern.edu/KeckII/ftir1.asp (May 20, 2007- 8 am).

[20] John R. Ferraro, in Fourier Transforms Infrared Spectroscopy, edited by Louis J. Basile (Academic Press, New York, 1978).

[21] E. Smith, in Modern Raman Spectroscopy: A Practical Approach, edited by G. Dent (John Wiley, Hoboken, NJ, 2005).

[22] H. Baranska, in Laser Raman Spectrometry, Analytical Application, edited by A. Labudzinska and J. Terpinski (John Wiley, New York, 1987).

[23] http://www.varianinc.com/cgi- bin/nav?products/spectr/uv/cary5000 /cary_5000&cid=JMPIINJLFI (May 14, 2007- 9 pm).

[24] http://www.osti.gov/bridge/servlets/purl/838021-Sirp9F/native/838021.pdf (April 01, 2007- 6 pm).

[25] J. P. Chatelon, C. Terrier, and J.A. Roger, Semicond. Sci. Technol. **14,** 642 (1999).

[26] S. Balaji, Y. Djaoued, and J. Robichaud, Raman Spectrosc. **37**, 1416 (2006).

[27] Y. Djaoued, S. Badilescu, and P.V. Ashrit, J. Sol-Gel. Sci. Technol. **24**, 247 (2002).

[28] T.J. Norman Jr., C.D. Grant, D. Magana, J.Z. Zhang, J. Liu, D. Cao, F. Bridges, and A.Van Buuren, J. Phys. Chem. B **106,** 7005 (2002).

[29] C. Xu, G. Xu, Y. Liu, X. Zhao, G. Wang, Scripta Mater. **46,** 789 (2002).

[30] R.D. Averitt, S. L. Westcott, N.J. Halas, J. Opt. Soc. Am. B **16**, 1824 (1999).

[31] M. Rumyantseva, A.M. Gaskok, N. Rosman, T. Pagnier, J.R. Morante, Chem. Mater. **17,** 893 (2005).

[32] L.J. Bellami, The Infrared Spectra of Complex Molecules, Vol. 2, 2nd ed. (Chapman and Hall, London, 1980).

[33] T.D. Senguttuvan and L.K. Malhotra, Thin Solid Films **289**, 22 (1996).

[34] M. Ristic, M. Ivanda, S. Popovic, and S. Music, J. Non-Cryst. Solids **303**, 270 (2002).

[35] H. Hövel, S. Fritz, A. Hilger, U. Kreibig, M. Vollmer, Phys. Rev. B **48**, 18178 (1993).

[36] E. D. Palik, Handbook of Optical Constants of Solids, Vol. 1, (Academic Press, Orlando, 1985).

[37] D. Davazoglou, Thin Solid Films **302**, 204 (1997).

[38] Y. Djaoued, S. Badilescu, P.V. Ashrit, D. Bersani, P.P. Lottici, and R.J. Bruning, J. Sol-Gel Sci. Technol. **24,** 247 (2002).

[39] S. Balaji, Y. Djaoued, and J. Robichaud, J. Raman Spectrosc. **37**, 1416 (2006).

[40] L.-J. Meng, V. Teixeira, H. N. Cui, F. Placido, Z. Xu, and M.P. dos Santos, Appl. Surf. Sci. **252**, 7970 (2006).

[41] N. Seirafianpour, S. Badilescu, R. Bruning, Y. D. Djaoued, S. Balaji, M. Kahrizi, and V.-V. Truong, "Optical Properties of Tin Dioxide-Coated Nanocrystalline Gold Films," Thirteenth Canadian Semiconductor Technology Conference, Montreal, Canada (2007).

[42] J. Elser, V. A. Podolskiy, I. Salakhutdinov, and I. Avrutsky, Appl. Phys. Lett. **90**, 191109 (2007).

[43] J. Elser, A. A. Govyadinov, I. Avrutsky, I. Salakhutdinov, and V. A. Podolskiy, Journal of Nanomaterials **2007**, 1-8 (2007).